Remote Sensing of Environment 328 (2025) 114896

Contents lists available at ScienceDirect

Remote Sensing of Environment

journal homepage: www.elsevier.com/locate/rse

Recent significant subseasonal fluctuations of supraglacial lakes on Greenland monitored by passive optical satellites☆

Jiahui Qiu [a,1], Jiangjun Ran [a,*], Natthachet Tangdamrongsub [b], Xavier Fettweis [c], Shoaib Ali [a], Wei Feng [d], Xiaoyun Wan [e]

[a] Department of Earth and Space Sciences, Southern University of Science and Technology, Shenzhen 518055, China
[b] Water Engineering and Management, School of Engineering and Technology, Asian Institute of Technology, Pathum Thani 12120, Thailand
[c] SPHERE research unit, Department of Geography, University of Liège, Liège 4000, Belgium
[d] School of Geospatial Engineering and Science, Sun Yat-Sen University, Zhuhai 519082, China
[e] School of Land Science and Technology, China University of Geosciences (Beijing), Beijing 100084, China

ARTICLE INFO

Edited by Menghua Wang

Keywords:
Greenland ice sheet
Supraglacial lakes
Deep learning
Google earth engine
Regional climate model

ABSTRACT

Temporarily impounded liquid water on the surface of the Greenland Ice Sheet (GrIS), prominently represented as supraglacial lakes (SGLs), may enhance ice flow and modulate surface meltwater runoff, serving as a dynamic indicator of the cryohydrologic cycle. Despite their importance in understanding glacier mass balance and regional climate change, a detailed description of SGLs and their intra-annual fluctuations across the entire GrIS remains understudied. Here, we present a deep learning-based approach to automatically map SGLs from passive optical satellite imagery across the entire GrIS during the melt seasons of 2017–2022. Approximately 150,000 Sentinel-2 and Landsat 8/9 images were utilized, each representing a 5-day average composite at a 10 km × 10 km grid resolution, with the Landsat images used as possible supplements. SGL predictions by the proposed method demonstrate high performance, achieving an F1-score of up to 0.959 compared to the independent test dataset. This high accuracy enables a detailed analysis of the key role SGLs play in enhancing surface ablation by absorbing solar radiation and delivering meltwater. The SGL-driven ablation effect was most pronounced in the South-West basin of the GrIS, where the peak lake area in July accounted for 44.9 % of the total GrIS-wide lake area. In contrast, the lowest magnitude (4.2 %) was observed in the South-East basin, despite similarly strong ablation in this region. Among all the generated SGL occurrence grids, peak SGL areas in certain grids (~14 % of the total) were observed in May or September, rather than exclusively during the typical high-ablation months of June to August, reflecting regional and elevation-dependent variations. Grids further from the ice sheet margin generally showed peak SGL areas later in the melt season, which is evident in the western part of the GrIS. Monthly SGL peak areas shift dramatically from 253.18 ± 123.94 km^2 to 5084.90 ± 1043.26 km^2, with the lowest in May 2018 and the highest in August 2021. An extraordinary area spike occurred in September 2022 and was particularly monitored in the South-West basin, where abnormally intense rainfall and runoff simulated by the Modèle Atmosphérique Régional (MAR) model were recorded. Our study highlights the significance of examining SGL area changes at short temporal intervals to understand the dynamics of cryospheric hydrology under future climate scenarios.

1. Introduction

Surface melting of the Greenland Ice Sheet (GrIS) has garnered significant scientific attention in recent years due to its potential implications for both global sea level rise and ocean thermohaline circulation (Stevens et al., 2015; van den Broeke et al., 2016; Smith et al., 2017; Ran et al., 2018; Banwell et al., 2019; van den Berk et al., 2021; Ran et al., 2024). Given the ongoing climate warming, compounded by the Arctic amplification effect, the mass imbalance of the GrIS has continued due to intensifying surface melting, with record-high losses in 2019 (−532

☆ This article is part of a Special issue entitled: 'Cryosphere remote sensin' published in Remote Sensing of Environment.

* Corresponding author.
E-mail address: ranjj@sustech.edu.cn (J. Ran).
[1] Present address: Water, Energy and Environmental Engineering Research Unit, University of Oulu, Oulu 90014, Finland.

https://doi.org/10.1016/j.rse.2025.114896
Received 27 October 2023; Received in revised form 25 June 2025; Accepted 30 June 2025
Available online 4 July 2025
0034-4257/© 2025 Elsevier Inc. All rights are reserved, including those for text and data mining, AI training, and similar technologies.

$\pm$ 58 Gt yr^{-1}) and 2012 (-464 ± 62 Gt yr^{-1}), highlighting the increasing severity of ice sheet mass loss in recent decades (Hanna et al., 2008; Fettweis et al., 2011; Nienow et al., 2017; Sasgen et al., 2020; Previdi et al., 2021).Widely dispersed meltwater is ephemerally impounded within surface depressions at the periphery of the ice sheet during the melt seasons, manifesting as supraglacial lakes (SGLs), supraglacial rivers, water-filled crevasses and moulins, as well as slushes, among others, collectively forming a complex cryohydrologic system (Chu, 2014; Yang and Li, 2014).

SGLs are a significant component of the total accumulated meltwater, densely clustered in the ablation zone across the GrIS, and play a crucial role in the drainage system, acting as key indicators of the cryohydrologic processes (Sundal et al., 2009; Ignéczi et al., 2016). The formation, drainage, and refreezing of SGLs influence surface runoff and glacial sliding, making them critical to understanding the dynamic mass loss from the ice sheet. Specifically, meltwater of certain SGLs could transport into the ocean through surface runoff, resulting in direct glacier mass loss (Colgan et al., 2011; Pitcher and Smith, 2019). Additionally, a portion of the surface meltwater infiltrates the ice sheet's interior via crevasses, reaching the ice-bedrock interface and enhancing basal lubrication, which leads to temporary acceleration in glacial sliding before subglacial drainage efficiency increases and moderates ice velocity (Zwally et al., 2002; Andrews et al., 2014; Dow et al., 2015; Chudley et al., 2019; Williams et al., 2020). The melting of the ice front also triggers calving events, which further contribute to mass loss through iceberg calving (van de Wal et al., 2008; Benn et al., 2017). Additionally, the contrast in surface albedo between SGLs and the surrounding ice surface facilitates marginal ice melting through positive feedback mechanisms, further amplifying meltwater production (Lüthje et al., 2006; Tedesco et al., 2012).

Multi-modal space-borne sensors, including passive and active microwave systems, along with sparse in situ measurements, have been employed to monitor large-scale melt processes and SGL dynamics, including the detection of lake extent, depth, and temporal evolution. One of the key challenges in tracking SGL evolution throughout the melt season is obtaining comprehensive and reliable satellite observations from multiple sensors. Passive optical satellite sensors can capture images with multiple spectral channels, and their relative ease of interpretation and valuable historical archives have led to the widespread utilization of optical imagery for SGL mapping. Specifically, using daily MODerate-resolution Imaging Spectroradiometer (MODIS) data and various band thresholding techniques, Selmes et al. (2011) mapped SGLs across the entire GrIS and quantified the proportion of suddenly drained lakes in each basin. Williamson et al. (2017) focused on two glaciers in West Greenland, developing an effective "FAST" algorithm to calculate the area and volume of SGLs. However, MODIS's inherent 250 m resolution is unlikely sufficient for capturing the intricate details of small and irregularly shaped SGLs. To address this limitation, advanced spatial resolution imagery from Landsat 8, Advanced Spaceborne Thermal Emission and Reflection Radiometer (ASTER), and Sentinel-2 were

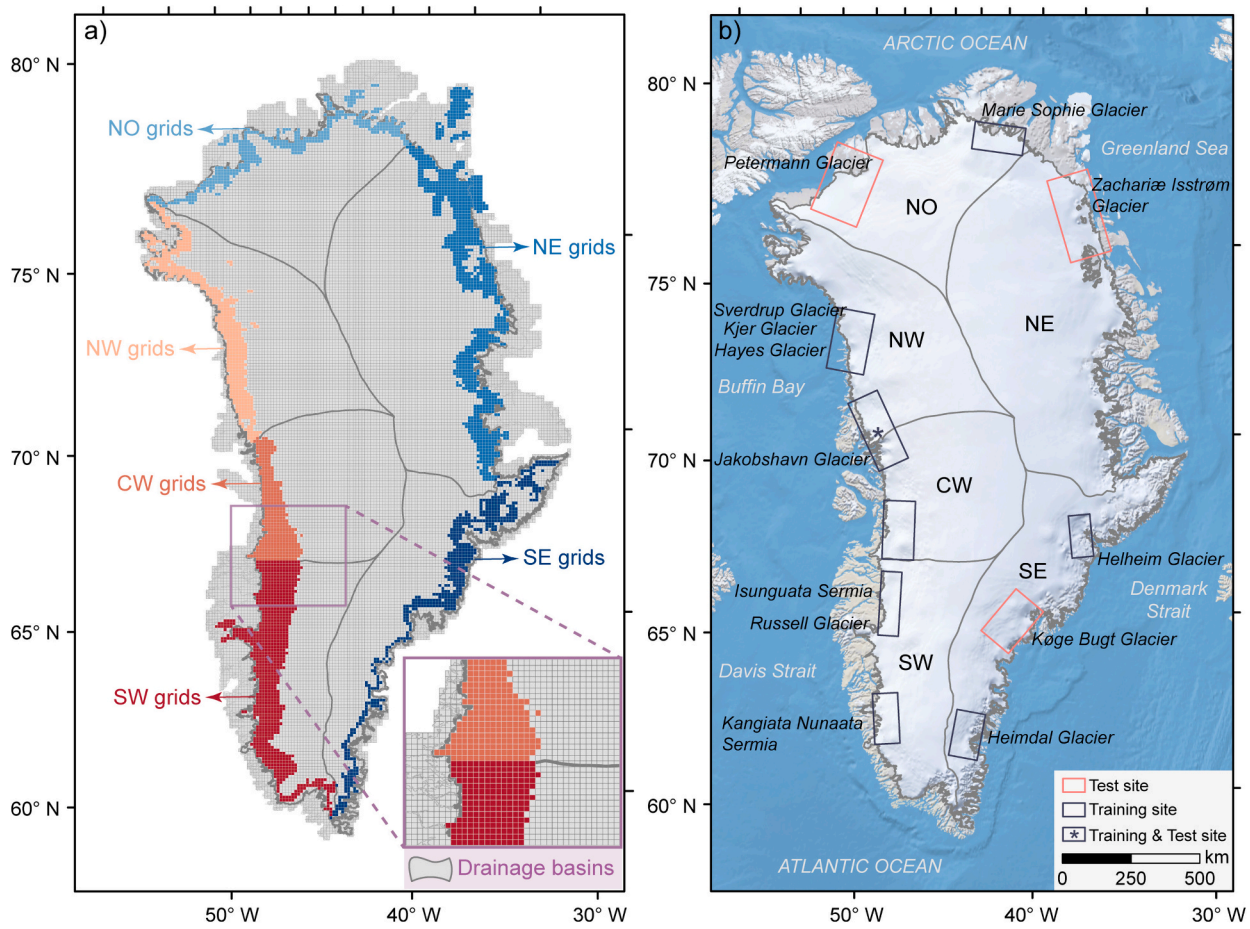

Fig. 1. a) 10-km SGL occurrence grid partition over the GrIS used as spatial constraints for satellite imagery archiving. A total of 3006 grids (blue-orange) were retained from an initial 21,799 grids (gray) generated by ArcGIS, based on manual visual discrimination using historical Landsat mosaic imagery from Chen et al. (2020). Gray lines outline six drainage basins, namely North (NO), North-East (NE), South-East (SE), South-West (SW), Center-West (CW), and North-West (NW), which are simply modified from Rignot and Mouginot (2012). b) Spatial distribution of training (gray-blue) and test (red) rectangular sites across the GrIS for selecting the optimal semantic segmentation model. The star indicates regions where both training and test data are available. (For interpretation of the references to colour in this figure legend, the reader is referred to the web version of this article.)

further used to extract SGLs at higher resolutions (up to 30 m, 15 m, and 10 m, respectively, for the Visible and Near-Infrared bands), based on a variety of water indices with different threshold constraints (Bell et al., 2017; Chen et al., 2017; Stokes et al., 2019; Moussavi et al., 2020;). In contrast, cloud-penetrating synthetic aperture radar (SAR) images were utilized in conjunction with different classification algorithms to detect perennial SGLs and winter drainage events in West Greenland (Miles et al., 2017; Benedek and Willis, 2021) and Northeast Greenland (Schröder et al., 2020). Though SAR-based approaches offer the advantage of being able to operate in all weather conditions for retrieving both supra- and sub-glacial lakes, the relatively low quality of imagery presents a formidable challenge in delineating SGLs accurately. Additionally, laser altimetry data from ICESat-2 photon clouds enable retrievals of SGL depth and volume (Fair et al., 2020; Datta and Wouters, 2021; Fricker et al., 2021), offering further insights into lake dynamics.

Conventional band ratio thresholds or machine learning methods, as applied in previous studies, may yield satisfactory results in particular regions. However, these approaches may lack the robustness and transferability required to map SGLs across the entire GrIS due to the complex and heterogeneous geometries of surface meltwater features, whereas CNN-based methods have demonstrated improved accuracy and adaptability across diverse glacial environments (Yuan et al., 2020; Jiang et al., 2022). In contrast, deep learning techniques, such as convolutional neural networks (CNNs), show great potential for accurately detecting SGL features from spaceborne imagery (Reichstein et al., 2019; Weiss et al., 2020). CNNs have proven effective in identifying cryohydrologic elements, including pro-, supra-, or sub-glacier lakes, across vast polar regions from both remotely sensed optical and SAR images (Dirscherl et al., 2020; Yuan et al., 2020; Hu et al., 2022; Jiang et al., 2022). Classical machine learning methods, such as Random Forest and Support Vector Machines, primarily rely on spectral information and may be simpler and more accessible through platforms like Google Earth Engine (Dell et al., 2021; Halberstadt et al., 2020). However, CNNs provide significant advantages by learning complex spatial and semantic patterns, producing outputs with less noise and fewer omission errors, particularly in outlining SGL bodies (Yuan et al., 2020). Despite these benefits, CNNs require more computational resources and training data, potentially increasing implementation costs. Nevertheless, an attempt to map dynamically changing SGLs across the entire GrIS with state-of-the-art algorithms is still warranted to better elucidate SGL distribution and its influence on mass balance. Furthermore, intra-annual and even subseasonal (with monthly peak values analyzed in this study) changes in SGL area variability at large scales have been inadequately constrained. A spatially and temporally explicit elaboration of SGL evolution is nontrivial but critically urgent for assessing the potential impacts on hydrological and ecological changes associated with the GrIS mass loss (Colgan et al., 2011).

Up to now, no dataset has described the highly dynamic fluctuations of SGL area across the entire GrIS at subweekly frequency. The primary aim of this study is to fill that gap by understanding SGL evolution at large spatial scales with high temporal resolution. To achieve this, we have set the following specific objectives: (1) Develop the best-performing semantic segmentation model through a series of sensitivity analyses on various in-house and classical CNN models; (2) map the extent of all SGLs across the entire GrIS at 5-day intervals from 149,055 processed 10 × 10 km image chunks derived from optical satellite scenes using the optimal model; (3) quantify both inter- and intra-annual changes in SGL peak area across the entire GrIS and within individual basins; and (4) analyze SGL dynamics from 2017 to 2022, incorporating simulated regional climate model outputs both spatially and temporally.

2. Study area

As the largest ice mass in the northern hemisphere, the GrIS is currently undergoing intensifying surface melting (Yang et al., 2018). In this study, we consider the entire GrIS for SGL mapping. Given the persistent cold conditions in the interior region of the GrIS, where any meltwater percolates into the snow and firn and refreezes, preventing the formation of SGLs, and considering the immense volume of remote sensing imagery, we applied spatial constraints to enhance computational efficiency. Specifically, we generated 10-km SGL occurrence grids based on historical cloud-free Landsat mosaic imagery to represent the potential extent of ponds. These grids were extended inward or outward, depending on geographic location, to minimize the risk of missing any potential SGLs and are primarily distributed along the periphery of the GrIS (Fig. 1a).

Morphologically diverse SGLs are distributed across all basins of the GrIS, and the presence of certain negative samples can interfere with the extraction accuracy as well as transferability of deep learning-based methods. In this regard, we ensured a geographically uniform distribution of training and test samples (Fig. 1b), taking into account various typical surface features, including lakes, streams, firns, crevasses, and bare ice. These samples were carefully selected to represent a broad range of glacier types from all drainage basins, ensuring comprehensive coverage of both positive examples (containing SGL pixels) and negative examples (consisting solely of background features without SGLs).

3. Data

3.1. Optical satellite imagery for SGL extraction

Passive optical images from the Sentinel-2 and Landsat 8 & 9 satellite missions were utilized to extract all SGL features across the entire GrIS. The wide swath Sentinel-2 constellation, equipped with Multi-Spectral Instrument (MSI) sensors, consists of two identical satellites, namely Sentinel-2A and Sentinel-2B, providing a high spatial resolution of 10 m and a revisit frequency of 5 days. To ensure sufficient orbit coverage over the GrIS region, we selected Sentinel-2 data from 2017 onwards (when Sentinel-2B became operational along with Sentinel-2A). Specifically, 308,534 images of MSI band-8 (Near-infrared band) Level-1C Top-of-Atmosphere Reflectance products were downloaded through Google Earth Engine (https://earthengine.google.com/), with original image tiles split into 10 × 10 km gridded images, to examine changes in SGL area during the melt season from 2017 to 2022 (Gorelick et al., 2017). We performed large-scale filtering based on imaging conditions, excluding images with invalid pixel counts greater than 20 % and those with overall dark tones that made discrimination impossible. Additionally, redundant images without lake pixels were removed at the beginning and end of the ablation season (May and September), retaining only one valid record per month in such cases. These filtering criteria resulted in a total of 149,055 images used in the analysis.

A carefully curated collection of Landsat 8 & 9 images (totaling 415) from Operational Land Imager (OLI) and OLI-2 sensors were purposefully selected to complement the Sentinel-2 archives, particularly in regions where SGLs were visually inspected to be prevalent. Landsat 8 data were used before 2022, while both Landsat 8 and Landsat 9 were incorporated during the summer of 2022 to improve coverage. Although these images have a slightly lower 30-m spatial resolution and a 16-day revisit frequency for each Landsat satellite, their combined use further reduces the revisit interval to 8 days, enhancing temporal coverage.

3.2. Auxiliary remote sensing products

We used the cloudless Landsat mosaic of Greenland obtained from Chen et al. (2020) as historical evidence of widespread and dynamic SGLs to constrain the number of 10-km grid cells that are computationally feasible with our limited resources. A total of 3006 SGL occurrence grids were generated using the “Create Fishnet” tool in ArcGIS, followed by thorough visual inspection and manual feature editing to remove redundant grids, with the majority located in the peripheral areas of the GrIS (Fig. 1a). Time averaged ArcticDEM (mosaic) data with

Table 1
Summary of remotely sensed datasets used in this study.

Satellite/ product	Time	Spatial resolution	Purpose
Sentinel-2 MSI	2017–2022	10 m	Map all SGL features using a single NIR band
Landsat 8 OLI & 9 OLI2	2017–2022	30 m	Complement for potential missing valid records of Sentinel-2 mission during the study period
ArcticDEM Version 3	released in 2018	2 m	Generate a slope mask and then apply it to mitigate the topographical impacts
GIMP Version 1.2	released in 2021	15 m	Apply GIMP ice masks at a gridded scale to accurately extract lakes on glaciers
Greenland mosaic	released in 2020	30 m	Generate SGL occurrence grids across the entire GrIS

a high spatial resolution (2 m) acquired from the Polar Geospatial Center (https://www.pgc.umn.edu/data/arcticdem/) were utilized for additional slope mask derivation to mitigate the effect of bedrock topography (Porter et al., 2018). Greenland Ice Mapping Project (GIMP) Ice & Ocean Mask obtained from Byrd Polar and Climate Research Center (https://byrd.osu.edu/research/groups/glacier-dynamics/data/icemask/) provides a binary raster of ice sheet mask at 15-m resolution (Howat et al., 2014), which can eliminate the issue of misclassifying ice-marginal ocean areas. Note that both the ArcticDEM-derived slope and the GIMP ice mask were cropped to the same 10 × 10 km grids as the satellite imagery.

Widely used six-basin division products developed by Rignot and Mouginot (2012) with slight modifications to make them compatible with grid outlines were then applied to gain a comprehensive understanding of the SGL area change within each drainage unit. Table 1 lists all the remotely sensed datasets used in this study.

3.3. Regional climate model simulations

Regional climate models play a crucial role in understanding the complex climatic processes that influence ice sheet dynamics, snow accumulation, and glacier mass balance, which are key factors in SGL formation. The Modèle Atmosphérique Régional (MAR) is a regional atmospheric model specifically designed for high-latitude regions like the GrIS. It serves as a valuable tool for simulating regional climate and generating multi-resolution meteorological data, aiding in the investigation of these processes in polar environments (Fettweis et al., 2017, 2020; Haacker et al., 2024). Here, a variety of daily outputs from MAR simulations (version 3.14, run at a spatial resolution of 15 km) were utilized to analyze the potential factors influencing SGL changes. These outputs include near-surface temperature (T2M), meltwater production (ME), rainfall (RF), runoff (RU), and surface mass balance (SMB). The simulations were forced every six hours by the ERA5 reanalysis to explain the correlation between SGL dynamics and atmospheric variations (Hersbach et al., 2020). MAR datasets can be accessed at http://ftp.climato.be/fettweis/MARv3.14/Greenland/.

4. Methods

4.1. Deep learning-based model for lake extraction

4.1.1. Pre-processing workflow

Similar to most classical semantic segmentation tasks and previous studies conducted (Dirscherl et al., 2020, 2021; Yuan et al., 2020; Hu et al., 2022; Jiang et al., 2022), we performed a series of procedures to prepare the satellite imagery data. We acquired all available Red-Green-Blue (RGB) composite and Near-Infrared (NIR) Sentinel-2 images during the melt seasons from 2017 to 2022, along with a small number of Landsat 8 & 9 images, based on the shapefiles of the designated training and test sites. When composited in true colour, SGLs exhibit a bluish or turquoise hue, contrasting sharply with the surrounding white ice/snow background. In contrast, in a single NIR band, SGL water bodies appear darker due to their strong absorption of longer-wavelength radiation, making them easily distinguishable from the brighter ice/snow surface. A stringent cloud cover threshold of 5 % was consistently enforced to minimize the impact of cloud shadows on the misidentification of lake water. To align Landsat images with Sentinel-2 image resolution, the native 30-m resolution was resampled to 10-m using the nearest neighbor sampling method. It is recommended to perform bulk cropping of larger-sized raw images when applying deep learning-based approaches, where different patch sizes have been employed in previous studies (Dirscherl et al., 2021; Jiang et al., 2022). In this study, we adopted subdivided 256 × 256 pixels patches to enhance the delineation of relatively small SGLs, considering the tradeoff between extraction effectiveness and data volume.

Both the RGB and NIR datasets contain 6057 patches, which were subsequently subjected to data augmentation, including rotation, flipping, and mirroring. This process yielded two final datasets, each containing 24,228 patches, for training and testing the model. In these datasets, 80 % of the samples were randomly assigned to the training set, while the remaining 20 % were reserved for the test set. Similar to Jiang et al. (2022), the entire dataset comprises a ratio of 1:2 between positive samples and negative samples. The corresponding ground truth labels were generated using the modified Normalized Difference Water Index ($NDWI_{ice}$) (Yang and Smith, 2013), combined with Otsu's auto-thresholding method (Otsu, 1979), which selects a threshold that minimizes intra-class variance. The SGL labels were further refined through detailed manual editing and visual interpretation to ensure accuracy.

4.1.2. Training semantic segmentation models

To evaluate the best semantic segmentation model for our task, we tested several models using two training-test datasets: one based on multi-band RGB data and another using single-band NIR data. The models included both our in-house network (LaeNet) and several widely-used architectures, namely Cloud-Net, U-net, UNet++, Deep-UNet, SegNet, AttResUNet, and AttSEResUNet (Ronneberger et al., 2015; Badrinarayanan et al., 2017; Li et al., 2017; Mohajerani and Saeedi, 2019; Zhou et al., 2019; Liu et al., 2021; Ouyang and Li, 2021; Wang et al., 2022).

These models differ in their architecture and approach to handling image features. For instance, U-net and its variants (UNet++, Deep-UNet) are popular for their use of skip connections, which allow the model to retain detailed spatial information (Ronneberger et al., 2015; Li et al., 2017; Zhou et al., 2019). The decoder in SegNet uniquely utilizes pooling indices from the max-pooling step of the corresponding encoder for efficient non-linear upsampling, optimizing computational resource usage (Mohajerani and Saeedi, 2019). Cloud-Net, on the other hand, is originally tailored for cloud detection in satellite images but was adapted for our SGL mapping task due to its robustness in identifying irregular shapes (Mohajerani and Saeedi, 2019). The attention-based models (AttResUNet, AttSEResUNet) incorporate attention mechanisms to focus on important image regions and feature channels, which improves accuracy when dealing with complex structures like SGLs (Ouyang and Li, 2021; Wang et al., 2022).

We adjusted three critical hyperparameters—learning rate (0.001), batch size (16), and epoch number (200)—to ensure optimal model performance. The learning rate controls how much the model weights change during training, while the batch size defines how many images are processed at once, and the epoch number indicates how many times the model processes the entire training set. To prevent overfitting and enhance model convergence, we also applied early stopping and learning rate decay. Detailed hyperparameter settings are provided in Table A1.

Among all the models tested, the AttSEResUNet model (Fig. A1), developed based on Wang et al. (2022), outperformed others in mapping

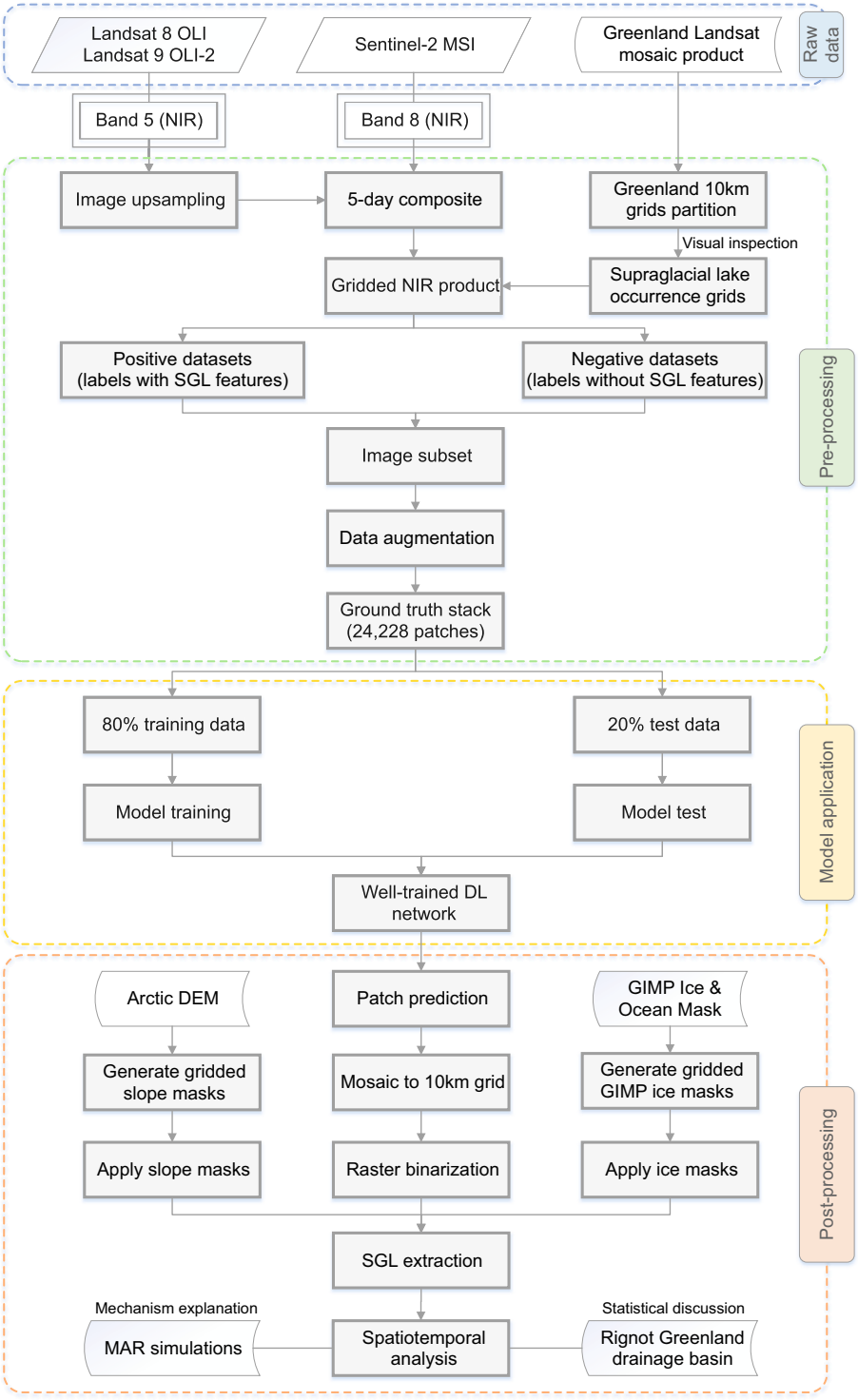

Fig. 2. Flowchart of automated SGL mapping from satellite imagery using a deep learning approach. Satellite imagery was archived on the Google Earth Engine platform. Model training was conducted in a GPU-accelerated environment, while image processing was implemented using Python programming.

SGLs due to the use of both spatial and channel attention mechanisms. Its ResUNet-based structure, with skip connections and residual blocks (Diakogiannis et al., 2020), captures both local and global contextual information. The self-gated attention module assigns varying weights to different spatial regions of interest, enhancing feature extraction. Additionally, the Squeeze-Excitation (S-E) block consists of a squeeze operation, which generates channel-wise statistics via global average pooling, and an excitation operation that learns their interdependencies (Hu et al., 2020). This allows the model to better detect subtle features, like pond water, at the pixel level.

4.1.3. *Post-processing workflow*

After the tuned model was established, over 2,390,000 patches were incorporated into the well-trained deep learning network for automatic prediction. All predicted outputs are grayscale images spanning a continuous range, devoid of geographic coordinates or projection information, requiring additional post-processing procedures. Initially, georeferencing was applied to align the predicted images with the

Table 2
Summary of evaluation metrics for all deep learning architectures tested.

	Accuracy	Precision	Recall	F1-Score	mIoU	Commission	Omission
U-net	0.996	0.899	0.971	0.933	0.936	0.004	0.029
LaeNet	0.982	0.830	0.528	0.634	0.729	0.003	0.467
SegNet	0.996	0.931	0.932	0.931	0.939	0.002	0.056
UNet++	0.994	0.921	0.884	0.901	0.908	0.002	0.116
DeepUNet	0.996	0.916	0.948	0.931	0.934	0.003	0.052
Cloud-Net	0.996	0.955	0.933	0.942	0.945	0.001	0.067
AttResUNet	0.997	0.951	0.943	0.947	0.948	0.002	0.057
AttSEResUNet	0.997	0.957	0.961	0.959	0.959	0.001	0.039

All the metrics listed here are derived from NIR datasets. For RGB dataset results, see Table A2.

original spatial reference of the input patches. Subsequently, these images were mosaicked into 10-km scenes corresponding to the generated SGL occurrence grids. To quantify the number of SGL pixels for lake area estimation, a fixed threshold value of 125 was employed to binarize the continuous grayscale predictions. This threshold corresponds to the widely adopted practice of applying a 0.5 threshold when binarizing predicted probability maps.

In addition, slope masks derived from ArcticDEM were applied to mitigate the impacts of steepness. Zones with slopes greater than 15°, as recommended by Jiang et al. (2022), were excluded to reduce shadow interference in the SGL mapping process. Moreover, ice masks provided by GIMP Ice & Ocean Mask were utilized to accurately extract lakes on glacier ice by disregarding non-ice pixels. To ensure consistency with the predicted results, the nominal spatial resolution of the applied GIMP ice mask (15 m) was further enhanced to 10 m using nearest neighbor sampling. The slope and ice masks were cropped into 10 km gridded products that coincided geographically with the generated SGL occurrence grids. Ultimately, the identified water pixels were tallied to quantify the SGL area within each grid, enabling us to estimate the SGL dynamics across the entire GrIS as well as the basin scale (as detailed in Fig. 2).

4.2. Accuracy assessment and uncertainty estimation

4.2.1. Accuracy assessment

Due to the scarcity of an independent SGL area dataset based on Sentinel-2 data, we used our manually refined, high-precision labeled test dataset, derived from the $NDWI_{ice}$ and Otsu thresholding process, to assess the performance of the different models. By applying performance criteria such as accuracy, precision, recall, F1-score, and mean Intersection over Union (mIoU), we were able to quantitatively evaluate the capabilities of different semantic segmentation models (Zhao et al., 2021). Moreover, both commission (i.e., non-SGL pixels identified as SGLs) and omission (i.e., SGL pixels identified as non-SGLs) errors were considered together to aid assessment (Pi et al., 2022). These metrics were calculated as follows:

$$Accuracy = \frac{TP + TN}{TP + TN + FP + FN} \tag{1}$$

$$Precision = \frac{TP}{TP + FP} \tag{2}$$

$$Recall = \frac{TP}{TP + FN} \tag{3}$$

$$F1\text{–}score = \frac{2 \times Precision \times Recall}{Precision + Recall} \tag{4}$$

$$mIoU = \frac{1}{2} \times \left(\frac{TP}{TP + FP + FN} + \frac{TN}{TN + FN + FP} \right) \tag{5}$$

$$Commission = \frac{FP}{FP + TP} \tag{6}$$

$$Omission = \frac{FN}{FN + TP} \tag{7}$$

where True Positive (TP), True Negative (TN), False Positive (FP), and False Negative (FN) are four components of the confusion matrix, which is a table that records the model's performance by comparing the predictions with the corresponding labeled masks for binary classification tasks.

Among these four components, TP and TN represent correct predictions, while FP and FN indicate incorrect predictions. In this study, TP refers to instances that were correctly predicted positive (SGL water), i.e., both the model predictions and the actual labels are positive classes. Similarly, TN denotes correctly predicted negative (all background) instances. In contrast, FP represents negative instances that were incorrectly predicted as positive, while FN represents positive instances that were incorrectly predicted as negative.

4.2.2. Uncertainty of the derived SGL area

Uncertainties in SGL mapping can be attributed to a variety of factors, including satellite imagery quality, deep learning algorithm reliability, auxiliary datasets accuracy, and post-processing procedures. These factors make it challenging, if not impossible, to provide a precise quantitative assessment of the uncertainties involved. In this study, we estimated the uncertainty of SGL area as the outer contour perimeter multiplied by half the image pixel size as eq. (8), a simple but feasible approach outlined by previous studies on area uncertainty estimation of glacial lake in the High Mountain Asia (Salerno et al., 2012; Zhang et al., 2023). Notably, certain morphological operations (i.e., majority filtering and boundary cleaning) were employed when deriving the SGL perimeter using the Zonal Geometry as Table function in ArcGIS. These operations help alleviate the effects of fine-grained plaques on contour extraction, which may lead to significant errors in calculating the SGL perimeter.

$$\partial A_i = P_i \times \frac{G}{2} \tag{8}$$

where ∂A_i is the uncertainty of SGL area, P_i is the corresponding perimeter, and G is the spatial resolution of satellite images (10 m pixel size here).

5. Results

5.1. Automatic SGL mapping from AttSEResUNet

We performed a series of experiments with two types of datasets (i.e., NIR and RGB datasets) to determine the optimal network for automatically extracting SGL from satellite images. As shown in Tables 2 & A2, AttSEResUNet consistently outperformed other networks for both NIR and RGB datasets, especially in terms of F1-score, which is of particular importance for binary classification scenarios. Nevertheless, the ultimate adopted strategy was to extract SGLs from NIR images using AttSEResUNet, given the comparable metrics conducted on both NIR and RGB datasets, as well as the immense data volume (approximately

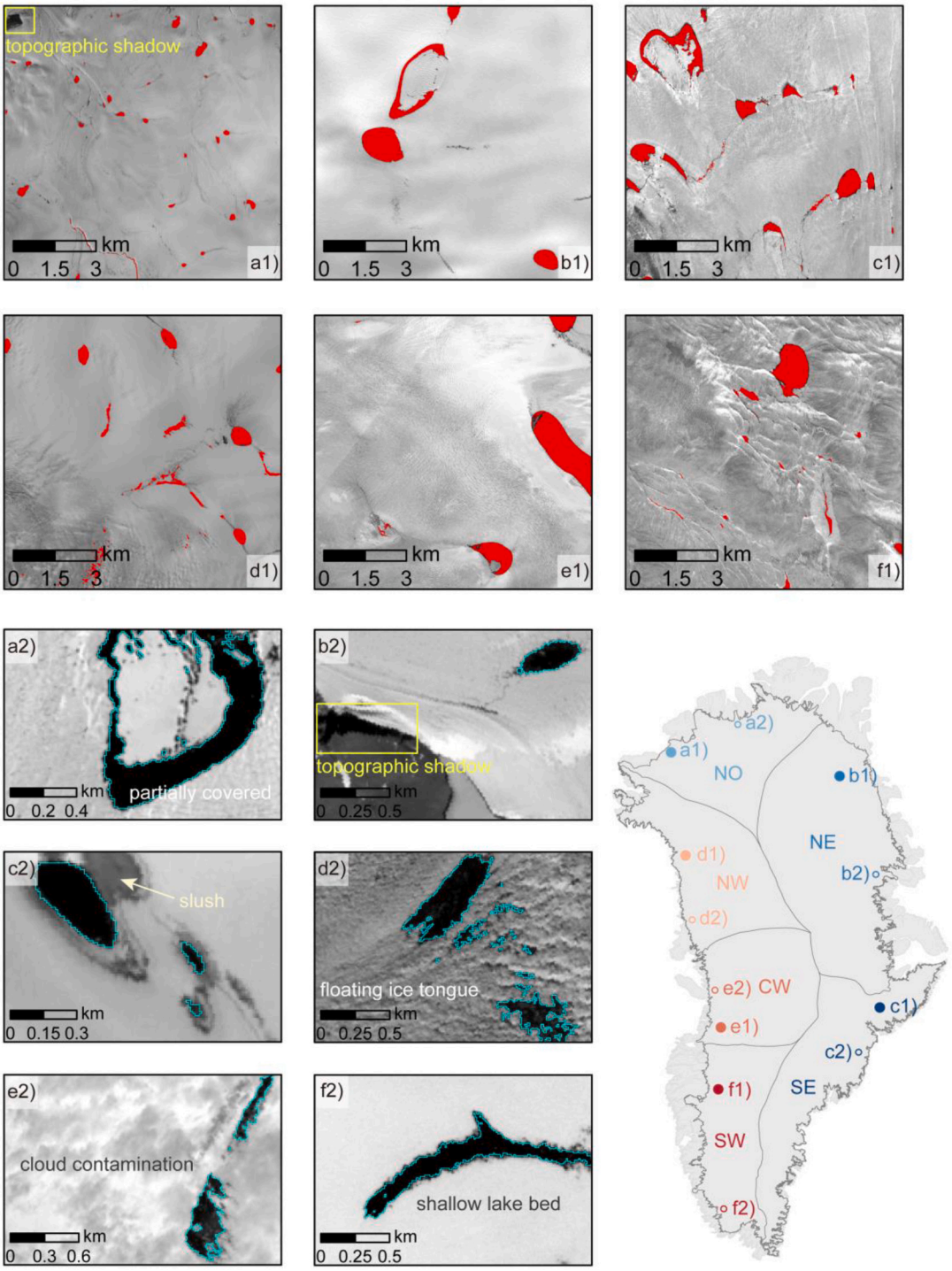

Fig. 3. The SGL extents mapped by AttSEResUNet model across six drainage basins. a1)-f1) illustrate SGL extraction at a 10 km gridded scale, corresponding to the large solid circles in each basin. a2)-f2) provide a detailed delineation of various SGL types under different conditions by outlining the predicted boundaries, corresponding to the small hollow circles in each basin.

150,000 images for NIR alone, with the RGB composite requiring three times the storage space due to its three image channels). Furthermore, an additional evaluation using entirely independent datasets from the year 2023—outside the training period and covering all representative regions, including both the red and black boxes in Fig. 1b—was conducted. The results further demonstrate the model's robustness and transferability across different temporal and spatial domains (see evaluation metrics in Tables A3 & A4).

SGLs can take on a variety of shapes, including arc-shaped (circular or oval), jagged, or elongated forms, which can be influenced by local topography, ice flow dynamics, and the underlying ice surface (Chu, 2014; Jiang et al., 2022). These lakes also vary in size from small ponds with diameters of a few dozen meters to large bodies of water spanning several kilometers in length. These variations in shape and size can impact the accuracy of lake identification, as the CNN algorithm must be able to recognize and delineate lakes in diverse forms. Nevertheless, the algorithm showed notable capabilities in SGL extraction, effectively handling variations in lake characteristics due to specific locations and

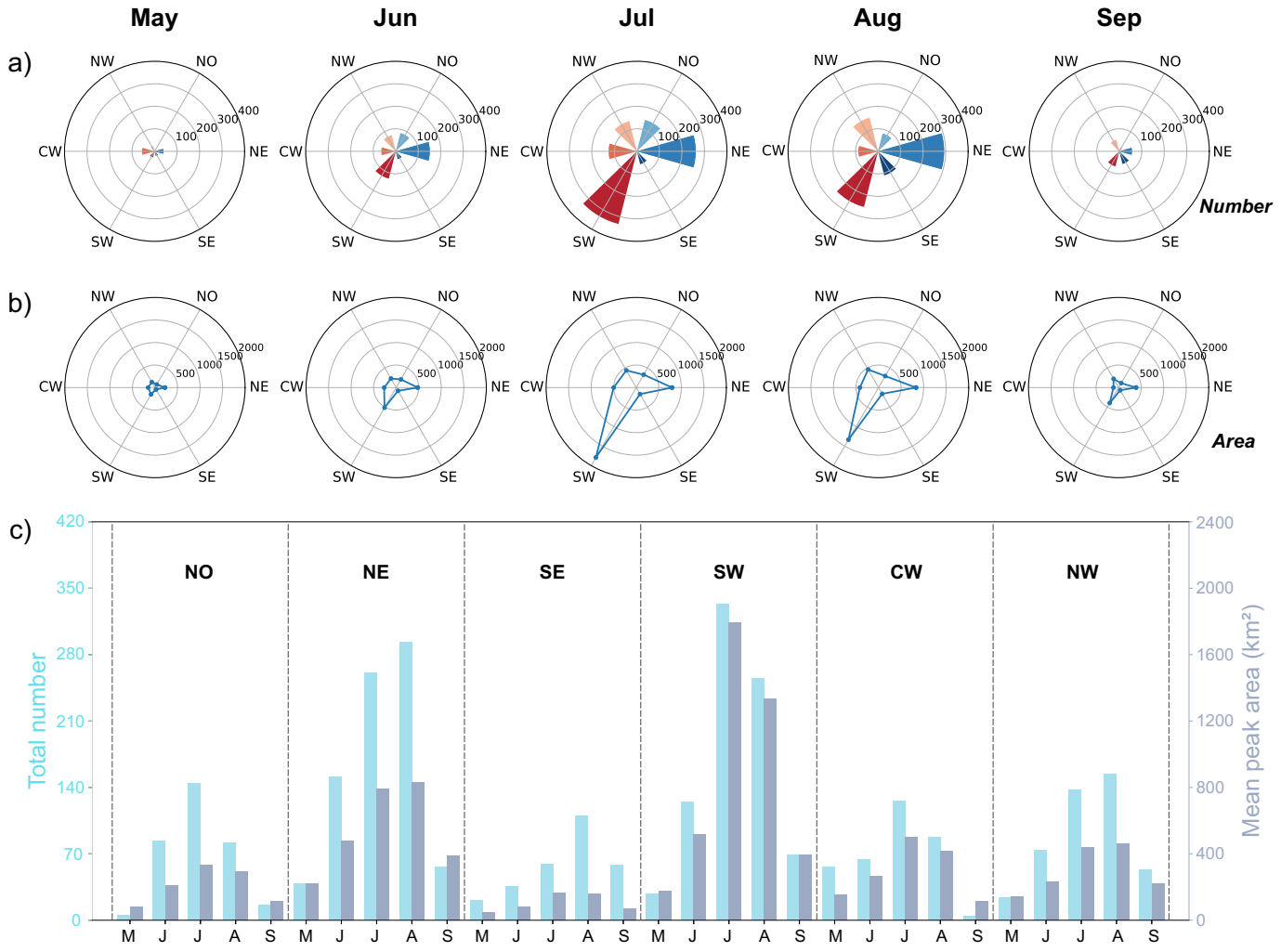

Fig. 4. Seasonal variations in the number and area of SGLs across six drainage basins. a) Total number of SGL occurrence grids reaching peak lake area from May to September. b) Sum of the mean monthly lake area (2017–2022) within each basin, unit in km^2. c) Histogram illustrating the monthly cycles of SGL grid numbers and areas.

hydrological conditions. These capabilities are highlighted through the SGL delineation results within six basins, presented at both a large scale (10 km grid cells) and pixel level (several tens of meters), as shown in Fig. 3.

Specifically, we identified 6 SGL grids that span the entire study period, are evenly distributed across all drainage basins, and exhibit distinct morphological features varying across different temporal and spatial contexts (Figs. 3 a1-f1 & A2). To provide a more detailed illustration, we employed a zoomed-in perspective to delineate the lake boundaries in 6 representative scenarios, which are SGLs with intricate shapes, affected by topographic shadows or wet slushes, located on floating ice tongues, contaminated by clouds, and with shallow lake beds, respectively (Fig. 3 a2-f2). Despite these challenges, the lake boundaries delineated by our deep learning-based method are well aligned with the actual shoreline, mitigating the potential effects of misclassification.

5.2. Drastic subseasonal fluctuation of SGL dynamics

To ensure the reliability of the area data and remove potential outliers caused by misclassification, we applied the three-sigma rule. Specifically, records that deviated beyond three standard deviations ($\mu \pm 3\sigma$) from the mean were excluded, assuming a near-normal distribution of area changes over time. Due to inconsistencies in image density and occasional gaps within certain months of the derived SGL area datasets, we focused on monthly peak area (hereafter simply area unless specified otherwise) for those SGL occurrence grids with continuous area records throughout the melt season. The monthly peak area represents the maximum total SGL area observed within each month for the respective SGL grids. For months lacking any valid records, the monthly peak value was defaulted to 0 to maintain data consistency.

To illustrate noticeable subseasonal changes in SGLs, we quantitatively evaluated the dynamics of number and area of SGL grids within each basin from May to September, as detailed in Fig. 4. Specifically, we presented the total number of SGL occurrence grids that reached area peaks, as well as the sum of long-term mean monthly SGL areas (averaged over 2017–2022), within each basin (Fig. 4a & b). The temporal changes in grid number and area exhibit a consistent pattern, with emergence in May, a surge in July, and nearly vanishing in September. Among all the drainage basins, the SW basin demonstrated the most pronounced changes in area, followed by the NE basin, while the SE basin exhibited the smallest changes despite exhibiting similar dynamic behavior (Fig. 4c).

The spatial distribution of grids with peak SGL area was mapped at both monthly and annual scales, and their corresponding frequencies were analyzed (Fig. 5). As shown in Figs. 5a & 6, peak SGL areas tend to occur later in the melt season as their location shifts further into the ice sheet interior at higher elevations. This pattern is particularly pronounced in the western basins (NW, CW, and SW), whereas greater stochasticity is observed in the eastern GrIS (Fig. A3). The observed

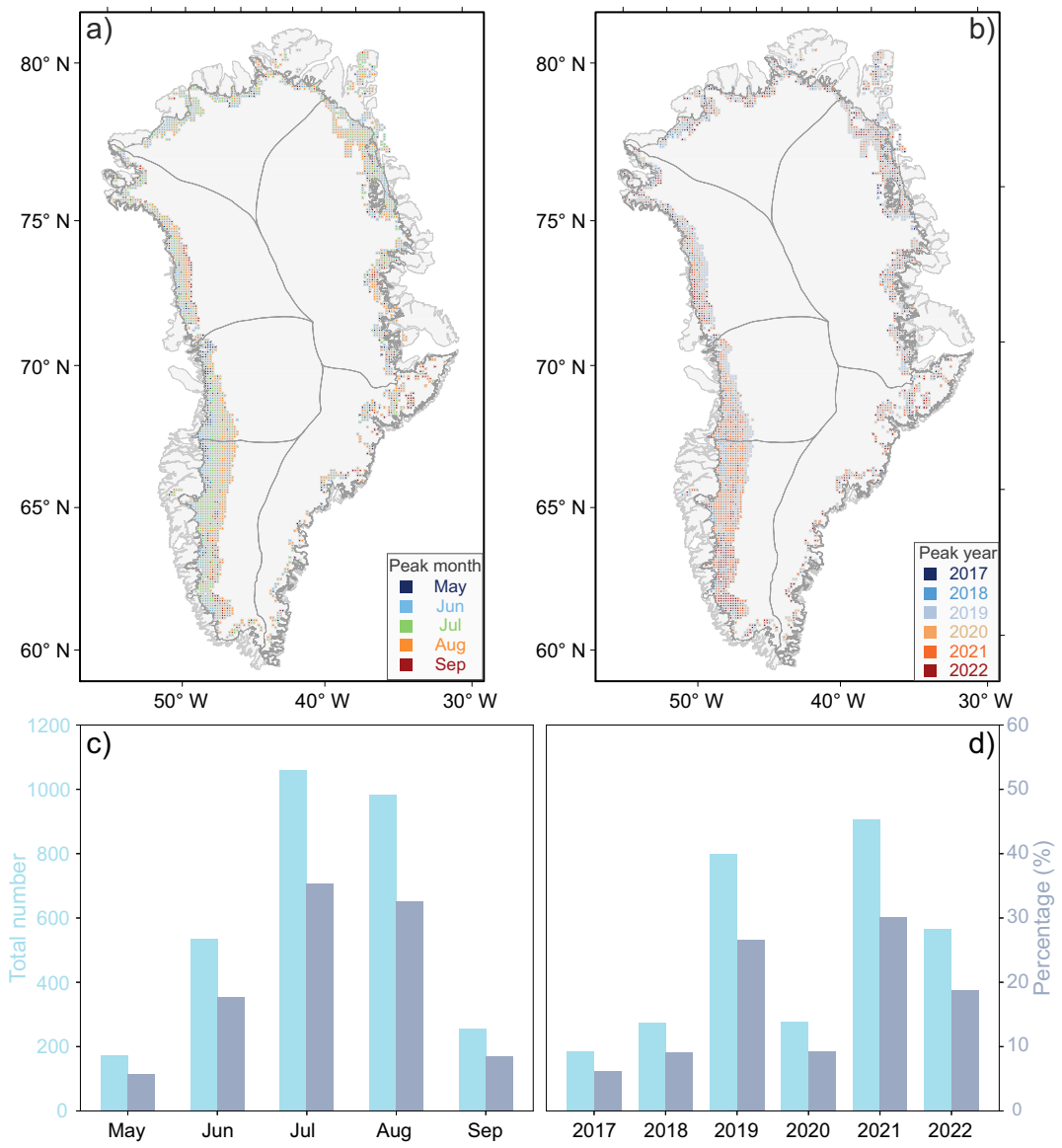

Fig. 5. The spatial distribution and frequency statistics of the SGL peak area. a) Distribution of SGL occurrence grids reaching their peak area on a monthly scale. b) Similar to a), but on an annual scale. c) Monthly and d) annual variations in the number of SGL occurrence grids reaching their respective peak lake areas.

relationship between peak area timing and ice surface elevation aligns with previous regional studies (Sundal et al., 2009) that reported similar trends in specific parts of the GrIS. However, our study extends these findings by providing a more comprehensive spatiotemporal perspective across the entire ice sheet. Additionally, Fig. 5b & d highlight 2019 and 2021 as the years with the most significant ablation effects, with peak SGL areas increasing by 47.43 % and 20.73 %, respectively, relative to the previous year, reaching 4588.01 km^2 and 5084.90 km^2. Notably, in approximately 14 % of the total grids, the peak month occurred in May or September, which typically marks the beginning or end of the melt season (Fig. 5a & c). The total SGL area in certain basins in September 2022 even exceeded that of August, an unexpected phenomenon in the time series that will be discussed later in *Sect. 6.1*.

The dynamics of SGLs within each grid were further assessed using two area thresholds: 1 km^2 and 5 km^2. Specifically, we categorized all SGL grids into two groups (i.e., small and medium) using a 1 km^2 threshold (see Fig. 7a & b). Medium SGLs ($\geq$1 km^2), although less frequent than small SGLs (<1 km^2) throughout the study period, played a significant role in driving the overall change in area across the entire GrIS. When a larger threshold of 5 km^2 was applied, a different variation pattern emerged (Fig. 7c & d). Moderate SGLs (<5 km^2) outnumbered large SGLs ($\geq$5 km^2) and demonstrated dominance in both area and particularly number. This pattern suggests a magnitude/frequency relationship, where smaller SGLs are more frequent but contribute less individually to the total area, while larger, less frequent SGLs have more significant impact on the overall area.

5.3. Comparison of remotely sensed SGL area with simulated MAR outputs

We quantified the subseasonal variability in SGL area at both regional (the entire GrIS) and local (individual drainage basin) scales. Additionally, we analyzed the daily outputs obtained from MAR simulations, which included key variables such as near-surface temperature, meltwater production, rainfall, runoff, and surface mass balance (Fig. 8). Due to the significant daily fluctuations of the MAR simulation, we further averaged the outputs to a monthly scale to better capture subseasonal variations. In general, meltwater production, near-surface temperature, rainfall, and runoff from the MAR simulations closely corresponded with SGL area variability. Notably, runoff showed a

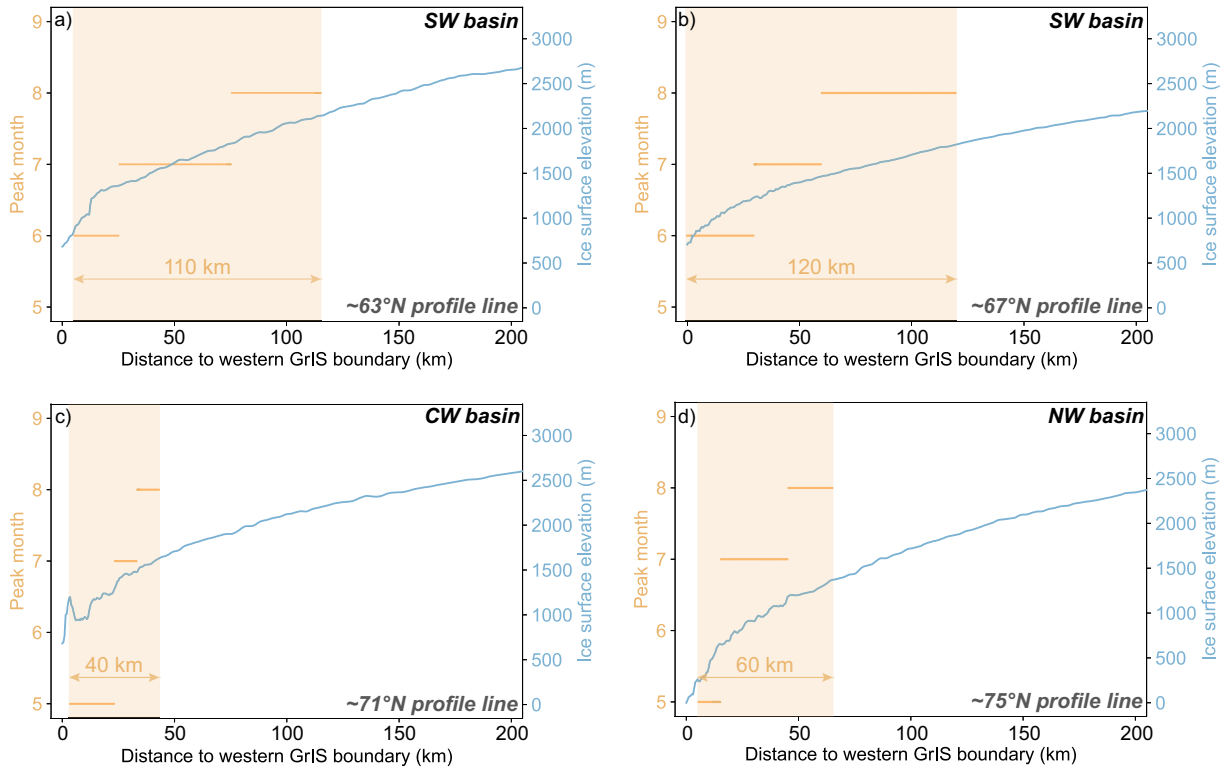

Fig. 6. Peak month (yellow) and ice surface elevation (blue) change with the distance to the western GrIS boundary. Light yellow columns indicate zones with SGL occurrence grids covered along four latitudinal profile lines spaced approximately 4° apart. Note that the maximum distance is truncated at 200 km to focus on the western basins (SW, CW, and NW), where spatial patterns are more distinct. (For interpretation of the references to colour in this figure legend, the reader is referred to the web version of this article.)

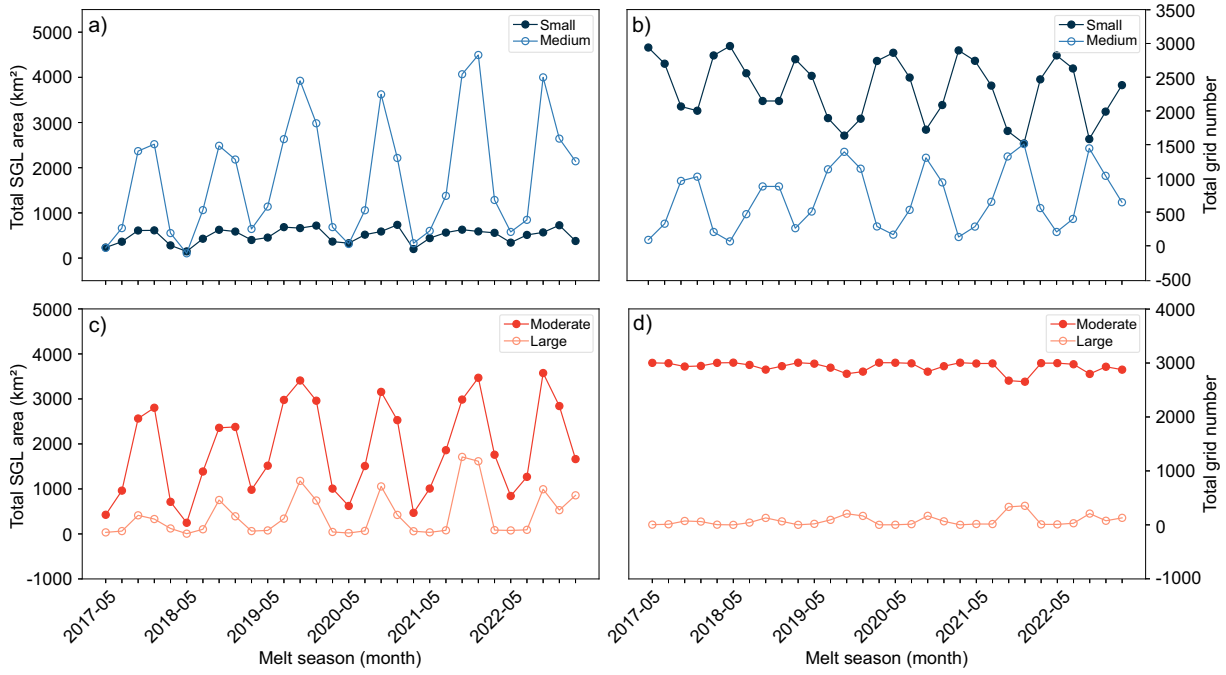

Fig. 7. Seasonal variations in total lake area and the number of grids reaching peak lake area during the melt season from 2017 to 2022. a) Total SGL area and b) grid number changes for small SGLs (<1 km^2) and medium SGLs (≥1 km^2). c) and d) Similar to a) and b) but with a larger area threshold (<5 km^2 for the moderate, ≥5 km^2 for the large).

particularly strong correlation with SGL area, with a Pearson correlation coefficient (r) of up to 0.92, indicating a robust positive relationship (Fig. 9). In contrast, surface mass balance displayed an almost inverse connection with SGL area, though less pronounced than that of -RU (negative runoff), with a Pearson correlation coefficient (r) of −0.90. This may be because SMB in summer is dominated by runoff and close to

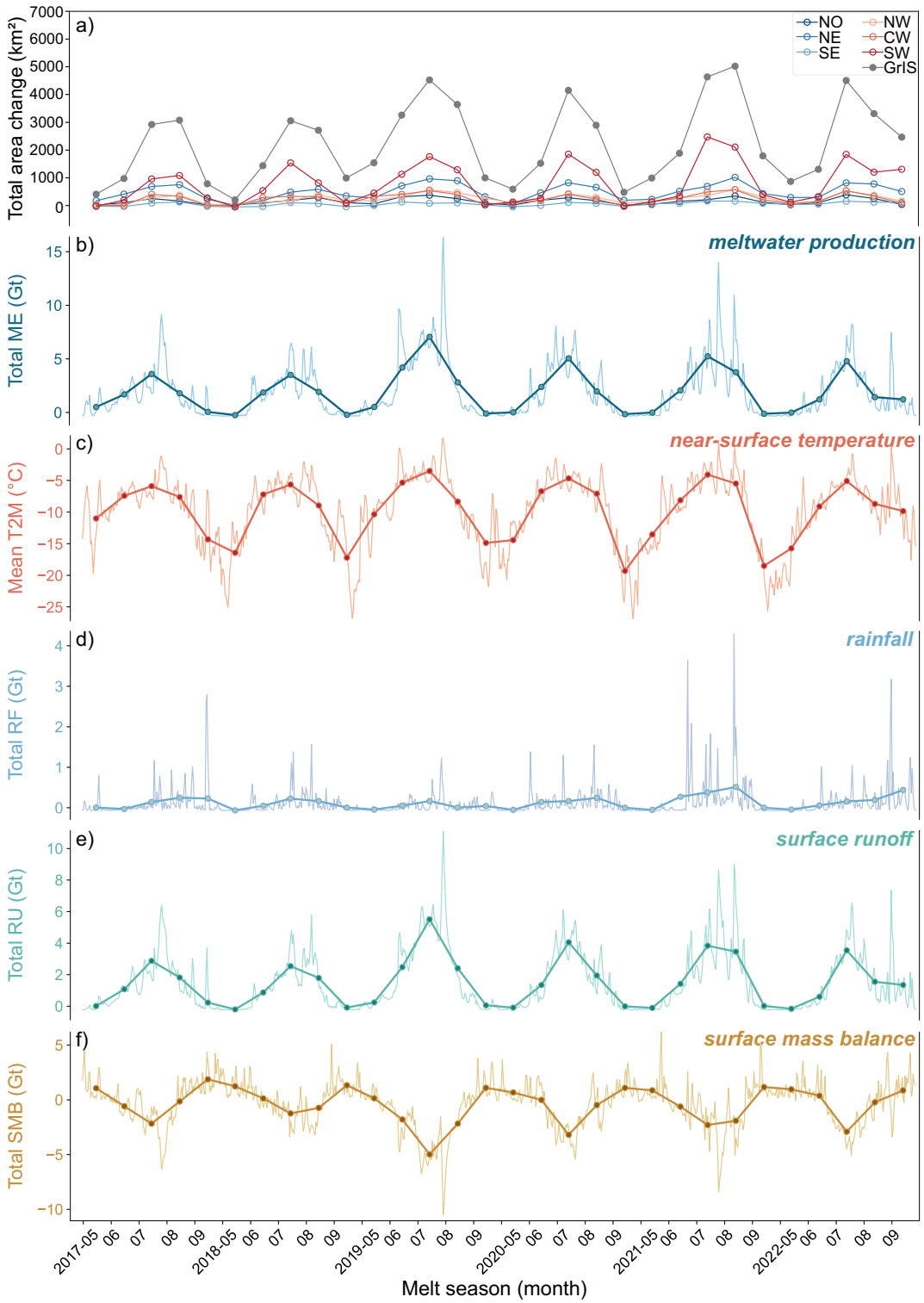

Fig. 8. Temporal variations in SGL area and MAR-simulated variables across the GrIS. a) Time series of total SGL area changes across the entire GrIS (solid circles) and within each basin (hollow circles). b)-f) MAR-simulated daily outputs (thin, light-colored lines) and their corresponding monthly averages (bold, dark-colored lines) for key variables over the entire GrIS. Total meltwater production, mean near-surface temperature, total rainfall, total runoff, and total surface mass balance are shown in b) to f), respectively.

-RU except inland (in the dry snow zone) where snowfall occurs, those snow accumulation however does not impact on SGLs (Fettweis et al., 2020). We note that the aforementioned lower correlations may also be attributed to the challenge of reasonably characterizing the highly dynamic daily outputs using monthly substitution.

The spatial distribution of monthly anomalies (relative to the melt season May to September from 2017 to 2022 period) were mapped for both observed SGL area and simulated RU from MAR to further examine the spatiotemporal characteristics (see Figs. 10 & 11). Additionally, the correlations between SGL area anomalies and anomalies in RU (Fig. 12), as well as other MAR variables (Fig. A4), have been analyzed across different years and months. It is important to note that RU represents the

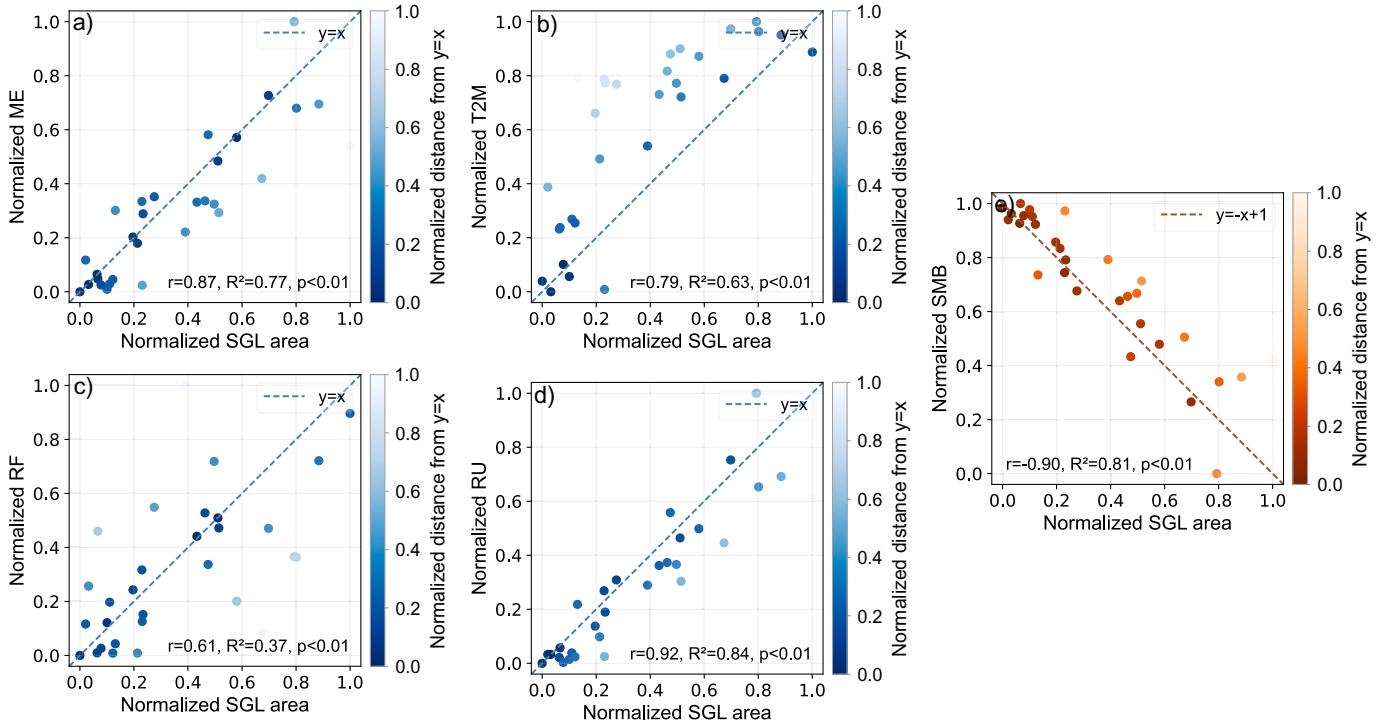

Fig. 9. Statistical correlation between monthly SGL area and five monthly averaged MAR outputs—ME, T2M, RF, RU, and SMB—is shown in a)–e), respectively. The dashed lines in each subplot represent lines with slopes of 1 or − 1. The proximity of data points to these lines reflects the strength of the positive or negative correlation, with darker colors indicating stronger correlations.

effective runoff of liquid water from meltwater, which can potentially fill the lakes. While liquid water from rainfall is not included in ME, and a portion of both ME and RF may be retained by the snowpack (Fettweis et al., 2020). Therefore, we exclusively used simulated RU for comparison with monitored lake area, rather than other water-related variables. Throughout the six-year ablation period, both SGL area and RU exhibit consistent spatial and temporal patterns, with a Pearson correlation coefficient (r) reaching up to 0.92, albeit with certain slight discrepancies observed. Eliminating potential calculation errors in both products, this consistency suggests that surface runoff plays a pivotal role in the formation and development of SGLs, with additional contributions from meltwater generated within the lake basins due to localized ice melting. Furthermore, it should be noted that the simulated runoff shown in Fig. 11 is constrained to be within SGL occurrence grids. While considering the potential impacts of spatially continuous MAR simulations on SGL evolution, we also assessed the related variables on a broader, regional scale (across the entire GrIS, not limited to SGL occurrence grids) and illustrated the anomalies for each component, as detailed in Figs. A5-A9.

The years 2019 and 2021 stand out as high melt years, as evidenced by the distribution of anomalies in the SGL area and the simulated runoff (Figs. 10 & 11). Remarkable positive anomalies were detected as early as June in 2019, with mean values of 0.43 km^2 for the SGL area anomaly and 4.27 mmWE/month for the RU anomaly. In contrast, similar positive anomalies emerged later in 2021, persisting until August, with mean values of 1.24 km^2 and 1.68 mmWE/month, respectively. The extended melt duration anomaly led to a greater total SGL area during the ablation period in these two years compared to others, reaching 4588.01 km^2 in 2019 and 5084.90 km^2 in 2021, as also evidenced by the concurrent increase in the number of SGL grids reaching their peak areas (Fig. 5d). High temperature anomalies through 2019 (Fig. A6) and heavy rainfall anomalies in 2021 (Fig. A7) are likely to be the main contributors to the increase in SGL impoundments in these two years, respectively. The high temperature anomaly in July 2019 reached up to 8.38 °C locally, while heavy rainfall anomalies in June, July, and August 2021 were as high as 6.60 mmWE locally. Exceptionally high amounts of melted water additionally contribute to the development of surface runoff, significantly impacting the mass balance of the ice sheet (Figs. A8 & A9).

The spatial distribution of each anomaly exhibits a distinct subseasonal (monthly scale in this study) pattern. Overall, for the SGL area, meltwater production, near-surface temperature, rainfall, and runoff, positive anomalies are predominantly observed during the high melt season, from June to August (Figs. 10, A5, A6, A7 & A8). In contrast, negative anomalies during this period are primarily found in surface mass balance (Fig. A9). These most significant anomalies generally occur in mid-melt season, particularly in July, which aligns with the peak in the SGL area time series. Subseasonal anomalies in near-surface temperature (Fig. A6) are more pronounced in the northern GrIS, whereas more conspicuous are observed in the southern GrIS for rainfall anomalies (Fig. A7). These results suggest that drivers behind SGL evolution are multifaceted and vary across different hydrologic regions, indicating a complex interplay of factors.

6. Discussion

6.1. Spatiotemporal characteristics of dynamic SGLs

Previous studies have examined some rapidly changing SGLs experiencing sudden drainage events, primarily using MODIS or Landsat imagery (Williamson et al., 2017; Christoffersen et al., 2018). However, these studies are limited to local scales or specific case studies, often covering only short melt periods. To date, no study has analyzed subseasonal changes in SGL area across the entire GrIS. Most related research focuses on interannual variations, providing only a single annual area estimate (Hu et al., 2022; Zheng et al., 2023). However, such yearly area may not be properly represented, given the rapid changes many SGLs undergo and the potential meltwater transportation through surface runoff or subglacial channels (Smith et al., 2017; Li et al., 2022). This complexity poses challenges for accurately calculating annual SGL areas using multi-phase satellite imagery mosaics. Besides,

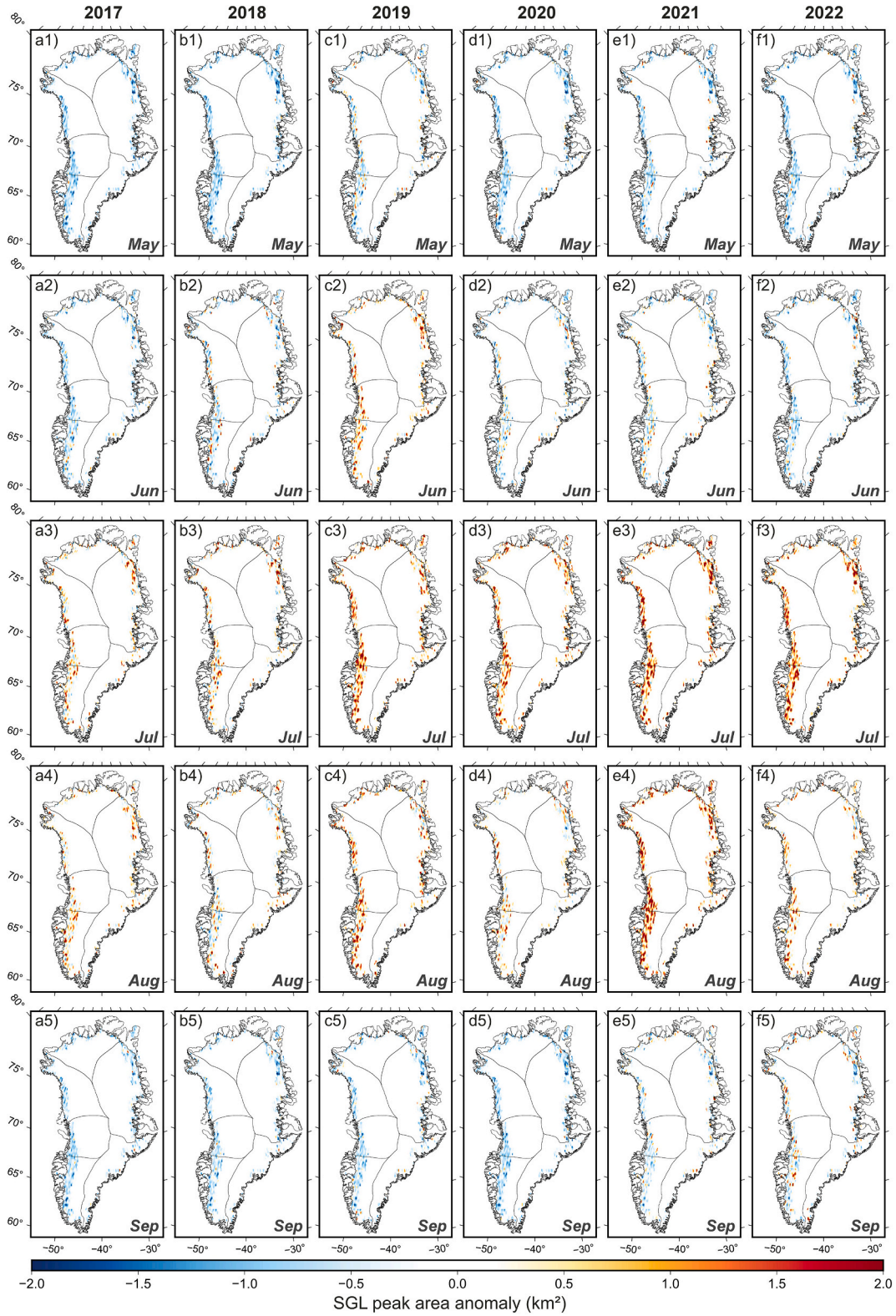

Fig. 10. Spatial distribution of observed SGL peak area anomalies across multiple melt seasons. a1)-a5) Monthly SGL peak area anomalies from May to September 2017. b1)-f5) Corresponding anomalies for the subsequent five years (2018–2022).

we here assumed that SGLs consist of at least 10 pixels at a 10-m spatial resolution, enabling the detection of even the smallest lakes, with areas as small as 0.001 km^2. This approach addresses the potential underestimation of SGL area in previous research.

Unlike the dominant pattern of SGL area variation (Fig. A10a), which generally peaks during the mid-melt season from June to August, fluctuations in ice surface elevation, drainage dynamics (Christoffersen et al., 2018), and abrupt climatic or hydrological shifts can lead to deviations from this regime (Fig. A10b & c). Particularly, an unprecedented late-season melt event was observed in September 2022, which,

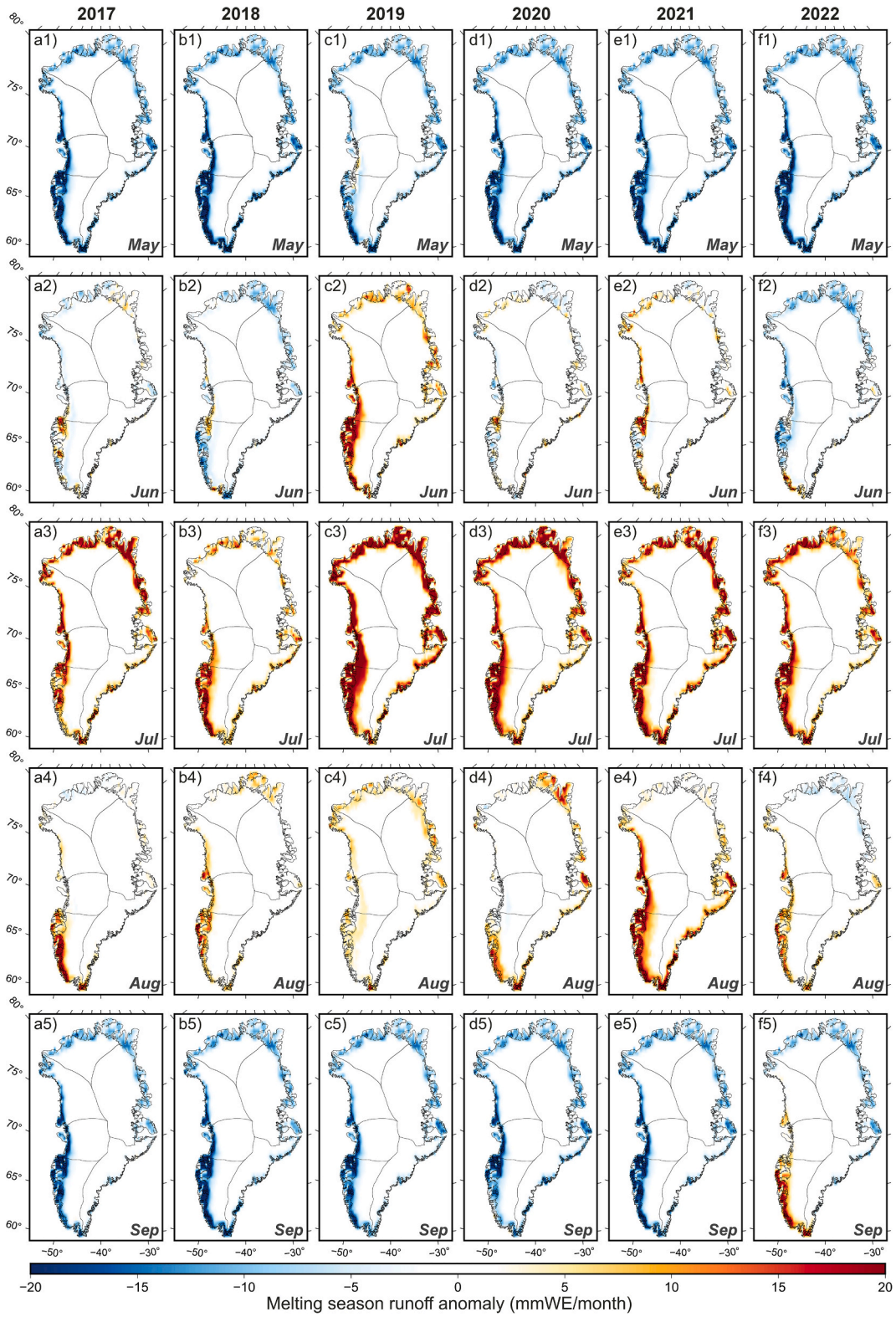

Fig. 11. Spatial distribution of simulated runoff anomalies from MAR. a1)-a5) Monthly runoff anomalies from May to September 2017. b1)-f5) Corresponding anomalies for the subsequent five years (2018–2022). To facilitate direct comparison with SGL area anomalies, the spatial extent is restricted to regions where SGL occurrence grids are present.

however, typically marks the end of the melt season. The melt spike was substantiated not only by the in situ meteorological observation records, as the Summit Station in Greenland experienced its first instance of exceeding the freezing point in September, but also by our findings that an unexpected increase of 105.16 km^2 in SGL area was observed in September 2022 in SW basin, rather than the anticipated decrease (refer to Figs. 5a, b, & 8a). Such late-season melt event may increase surface runoff the following summer, as refrozen water lenses can impede the infiltration of meltwater into the ice surface, potentially redirecting it toward the ocean (Moon et al., 2022).

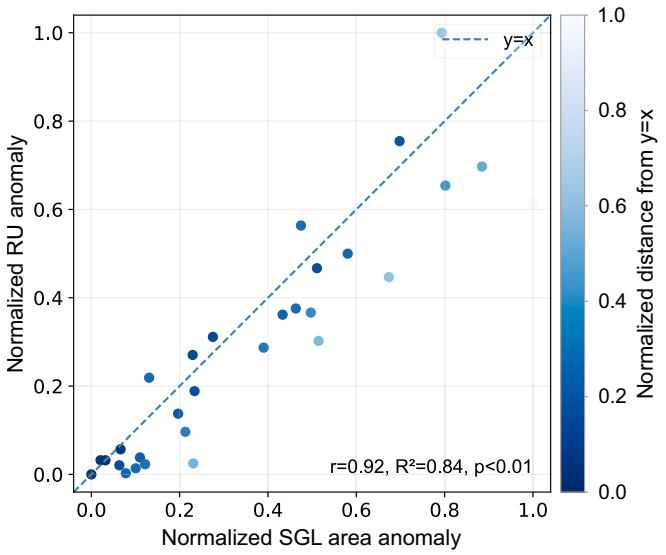

Fig. 12. Statistical correlation between monthly SGL area anomalies and monthly RU anomalies. The proximity of data points to the dashed lines reflects the strength of the positive correlation, with darker colors indicating stronger correlations.

Intensive clustering of small-sized SGLs with rapid changes in extent was primarily observed in the vicinity of the Nioghalvfjerdsfjorden glacier (also known as 79 N Glacier) and Zachariae Isstrøm glacier (ZI Glacier) in the NE basin, which represent as the most significant region of ice discharging in northern Greenland (Beyer et al., 2018; Turton et al., 2021). This phenomenon was particularly prominent on the floating ice tongue, which efficiently drains meltwater through rivers or crevasses, and it was also accompanied by rift formation at the terminus of marine-terminating glaciers, as shown in Fig. 13. Meanwhile, this may also be the reason why, during the high ablation months of July and August, the NE basin has a comparable or even higher number but a significantly smaller total area of lakes (794.30 km^2 in July and 831.46 km^2 in August) —about half that of the SW basin (1806.58 km^2 in July and 1335.77 km^2 in August), which experiences the most pronounced thawing effect, as illustrated in Fig. 4. Moreover, the density and intensity of SGL observed in the SE basin are relatively less pronounced, accounting for only 4.58 % of the total GrIS, despite the region contributing a substantial proportion (29.74 %) of the simulated meltwater production (Fig. 14) compared to other basins. This can likely be attributed to the heavy runoff (Fig. A11) and rapid drainage events prevalent within this locality, as the SE basin is characterized by a relatively steep ice surface, a relatively narrow ablation zone, and its proximity to the ocean (Sundal et al., 2009). This leads to the formation of subglacial drainage systems and, on average, rapid water release into the ocean, despite the widespread presence of firn aquifers (Ran et al., 2024). Further research is needed to shed more light on these regional hydrological differences.

6.2. Validation against previous studies and operational datasets

After establishing the significant spatiotemporal correlation between SGL area and multiple MAR simulations, we further validated the reliability of our results by comparing the monthly SGL peak area with previous research and related operational datasets (Fig. A12). Specifically, two relevant studies (Hu et al., 2022; Zheng et al., 2023) provide annual estimates of SGL extent across the entire GrIS. For the years directly comparable to this study, our monthly area estimates are of a similar magnitude to the annual estimates reported by Hu et al. (2022). However, Zheng et al. (2023) reported significantly smaller summer SGL areas, averaging only about one-third of those estimated in this study.

Additionally, we compared the monthly SGL area with the Joint Research Centre's (JRC) Global Surface Water (GSW) dataset, which is derived from 30 m resolution Landsat imagery and provides global surface water extent from 1984 to 2021 (Pekel et al., 2016). Notably, the JRC Monthly Water History dataset derived from GSW does not differentiate between proglacial and supraglacial lakes and primarily captures surface water near the ice sheet margins, particularly in the southwestern basin, while offering limited valid data for the ice sheet interior. Consequently, the JRC Monthly Water History dataset tends to underestimate the total SGL area during the melt season compared to our SGL area dataset. Nevertheless, the JRC Monthly Water History dataset remains a valuable global reference for monthly surface water extent, and its relatively lower performance in SGL mapping is understandable given its broader scope.

We also incorporated the MEaSUREs Polar EASE-Grid 2.0 Daily 6 km Land Freeze/Thaw (F/T) Status dataset from AMSR-E and AMSR2, Version 2, which provides global daily F/T status at a 6 km resolution (Kim et al., 2021). For our analysis, we examined the once-per-day composite (CO) classification data from May to September during the 2017–2021 period (with data available until the end of 2021). To enable a direct comparison with our monthly SGL peak area, we extracted the monthly peak thawed area within the study period. Both datasets exhibit distinct subseasonal variability, with peak areas occurring during the high melt season (July or August). However, due to the coarser 6 km resolution of the F/T dataset, its estimated thawed area is, on average, approximately 70 times larger than the SGL area derived from Sentinel-2 at a 10 m resolution.

Despite these differences, the SGL area estimated in this study demonstrates a strong correlation with both operational datasets. The Pearson correlation coefficient (r) and coefficient of determination (R^2) are 0.83 and 0.68, respectively, when compared with the JRC Monthly Water History dataset, and 0.83 and 0.69 when compared with the F/T dataset, both of which are statistically significant ($p < 0.01$).

6.3. Limitations and prospects

Automatic mapping SGLs from gridded passive remotely sensed imagery using a deep learning approach yields promising results (see *Sect. 5.1*). Compared to traditional machine learning methods like Random Forests or Support Vector Machines, CNNs demonstrate superior performance, producing less noise and fewer omission errors due to their ability to capture complex spatial and semantic patterns (Yuan et al., 2020). However, some limitations remain, including difficulties in distinguishing SGLs from spectrally similar features, such as slush or blue ice, challenges in the CNN model's ability to learn spectral and semantic information, and inconsistencies in reflectance caused by variations in solar illumination.

Misidentifications of certain linear features (e.g., supraglacial rivers and their tributaries) persist, likely due to the presence of an insufficient number of negative examples or incorrectly labeled samples (Zhang et al., 2021). Adding more accurate training samples and corresponding ground truth labels may help mitigate these issues and further reduce the relatively high omission error (3.9 %). Considering the tradeoff between extraction accuracy and limited computational and storage capacity, the SGL mapping strategy in this study was established by utilizing AttSEResUNet and single-band NIR imagery. However, this approach may not fully exploit the potential of AttSEResUNet's differential sensitivity to each channel. Therefore, considering the integration of multi-band imagery and other information, such as DEM, is a promising enhancement (Zhang et al., 2021).

Furthermore, setting a stringent cloud cover threshold may lead to the potential absence of valid optical imagery during overcast conditions, complicating time series analysis on a sub-monthly scale. To address this, incorporating cloud-penetrating SAR imagery could expand the dataset and improve temporal coverage (Benedek and Willis, 2021; Jiang et al., 2022). Despite the current data sampling density

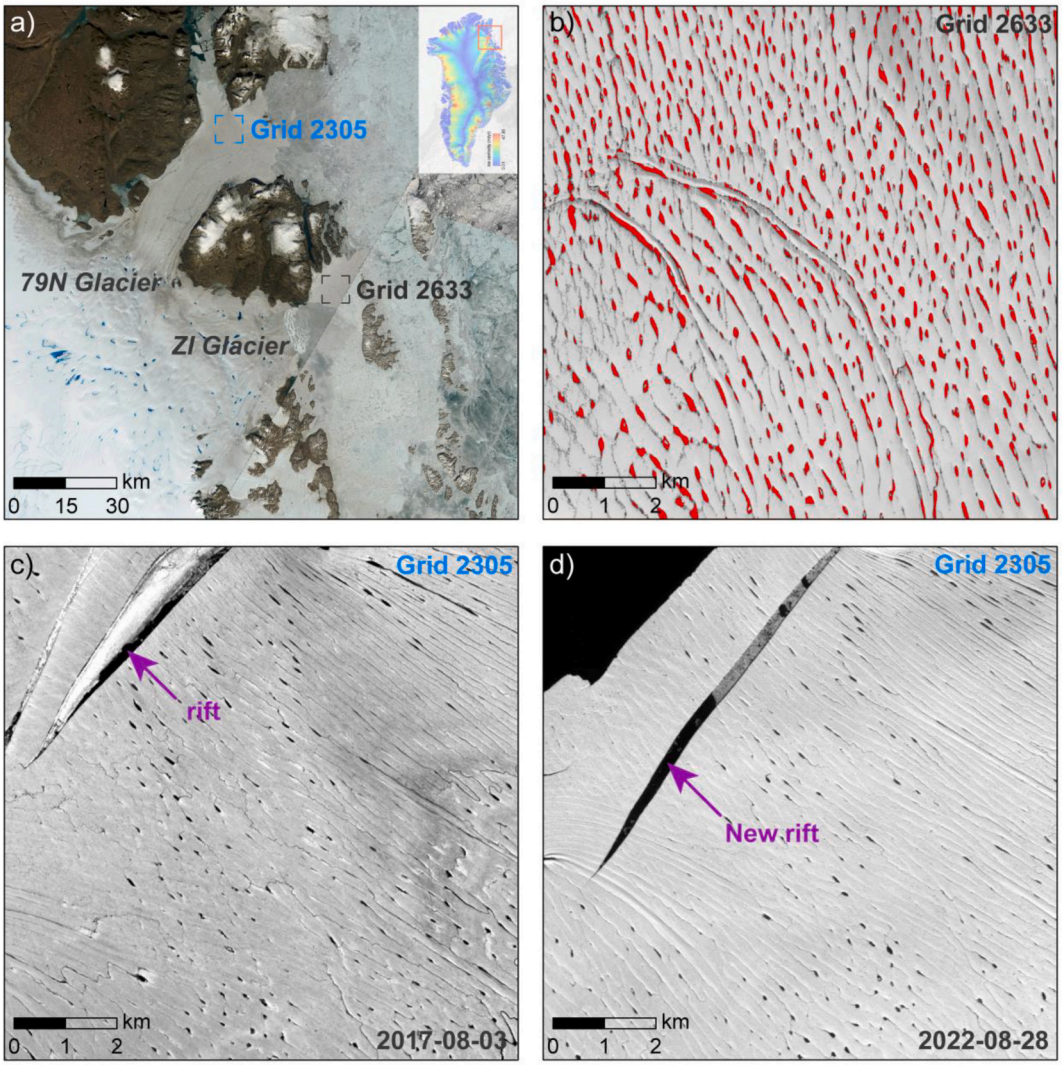

Fig. 13. Extensively distributed and fast-changing SGLs in the NE basin. a) Zoomed-in view of two significant floating ice tongues in the NE basin: 79 N Glacier and ZI Glacier. The inset in the top-right corner displays mean ice flow velocities from 1985 to 2018 (Gardner et al., 2018). b) Map showing intensive clustering of small SGLs on the ice tongue, which is attached to the front of marine-terminated ZI Glacier, corresponding to the black dashed box in a). c) and d) Evolution of fast-changing SGLs and the terminus glacier mass loss at the front of 79 N Glacier, corresponding to the blue dashed box in a). (For interpretation of the references to colour in this figure legend, the reader is referred to the web version of this article.)

(averaged over 5 days), certain rapidly evolving and short-lived SGLs, which may drain within hours to days, remain difficult to capture (Christoffersen et al., 2018; Li et al., 2022). Additionally, averaging over 5-day periods can introduce blurring effects in fast-flowing areas (e.g., floating ice tongues and particularly tabular icebergs) and topographically influenced regions. Utilizing scene-by- scene SGL mapping, given the relatively short revisit time of satellites, would reduce these blurring effects (Christoffersen et al., 2018).

The formation and development of SGLs are primarily controlled by localized topography and surface melting, with the latter being modulated by atmospheric circulation patterns. However, when further quantifying SGL water mass changes—encompassing both storage and drainage processes—and comparing them with satellite gravity-based measurements, impoundment depth information is the prerequisite for SGL volume or mass estimation (Lampkin et al., 2020). While ICESat-2 photon clouds can measure supraglacial pond depth with high precision, this method is limited to the satellite's ground track (Datta and Wouters, 2021; Fricker et al., 2021). Alternatively, both physically based (Pope, 2016) and empirical power-law-based methods (Williamson et al., 2018) offer the ability to estimate lake depth for all water pixels, though accuracy challenges may exist. Nonetheless, these approaches provide a viable attempt for regional assessment of lake depth or volume across the entire GrIS.

7. Conclusion

A meticulous characterization of subseasonal SGL area dynamics across the entire GrIS is important yet remains limited in investigation. In this study, we utilized approximately 150,000 passive remote sensing images from multi-source satellite observations, specifically Sentinel-2 and Landsat 8/9, spanning the 2017–2022 melt seasons. To automatically map SGLs, we employed a dual attention-based convolutional neural network (AttSEResUNet), which achieved high validation accuracy with an F1-score of 0.959 against independent test labels. We conducted a comprehensive analysis of monthly subseasonal variations in SGL areas across the entire GrIS and spatiotemporally examined relevant MAR model simulations, including near-surface temperature, rainfall, runoff, surface mass balance, and other variables to explain the SGL evolution patterns.

More than half of SGL occurrence grids (a total of 3006) recorded peak lake areas of less than 1 km^2, even on a 10 km × 10 km grid scale. Only a small portion (approximately 10 %) of these grids exhibited peak

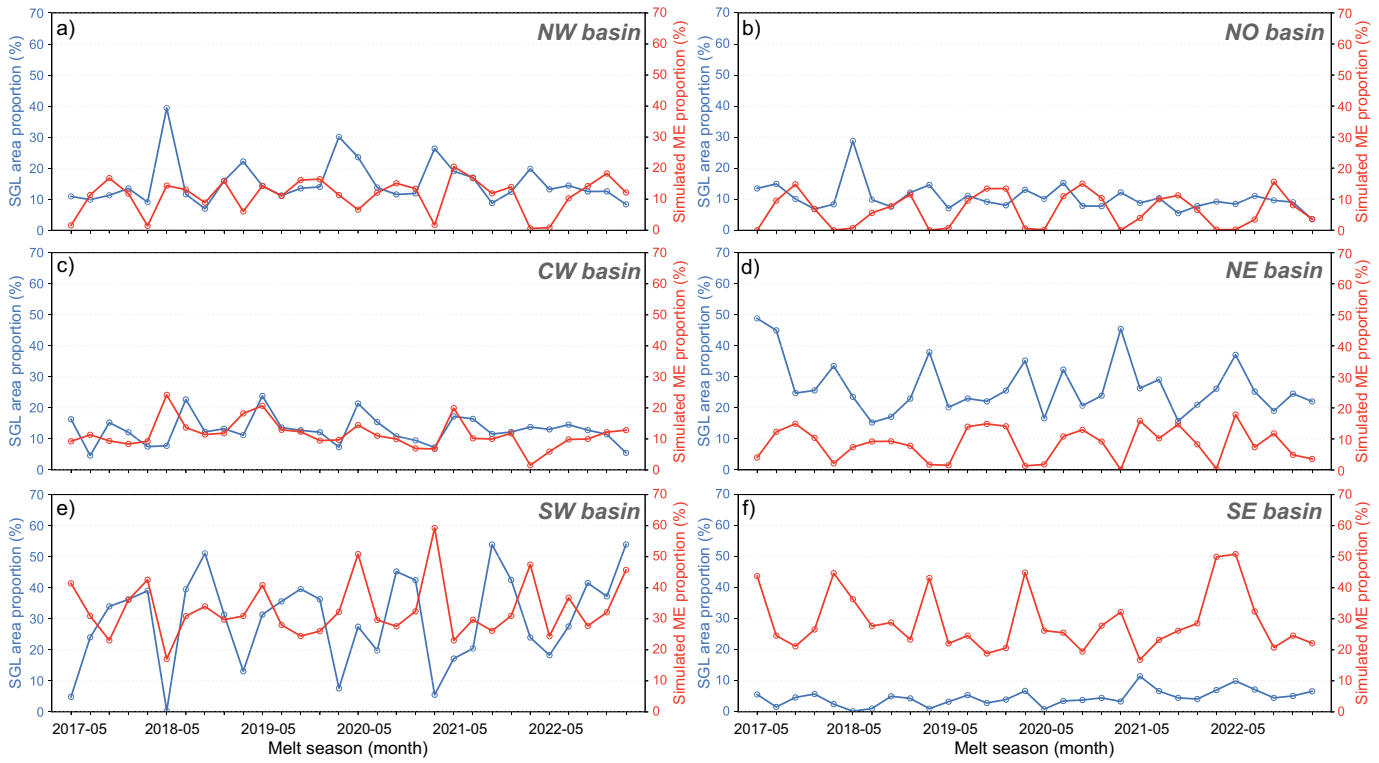

Fig. 14. Proportion of observed SGL area (blue) and simulated ME (red) within each basin relative to the total across the entire GrIS. Proportions in NW, NO, CW, NE, SW, and SE basins are shown in a) to f), respectively. (For interpretation of the references to colour in this figure legend, the reader is referred to the web version of this article.)

SGL area greater than 5 km^2. Each drainage basin experiences significant subseasonal variations, with peak areas predominantly occurring in the mid-melt season of July. The SW basin exhibited the largest magnitude, accounting for 44.9 % of the total SGL peak area, followed by the NE basin, with the NW and CW basins trailing closely behind. In contrast, the SE basin contributed only 4.2 % to the total peak SGL area, despite MAR simulations indicating similar levels of meltwater production as in the SW basin. These SGL area fluctuations were largely driven by atmospheric forcing, as evidenced by the concurrent anomalous changes in the SGL area and several MAR variables, along with their high correlations.

Our study provides a large-scale, high-spatial-resolution, and short-time-interval SGL area dataset from the recent 6 years, capable of measuring ponds as small as 0.001 km^2 and capturing significant changes in SGL area, which potentially alleviates concerns of previous underestimations (Hu et al., 2022; Zheng et al., 2023). Most importantly, it serves as a gateway to improved understanding of SGL dynamics across the GrIS at the subseasonal scale. Further work through interdisciplinary collaboration is needed to investigate subseasonal mass changes of SGL-included surface meltwater in order to forecast the future behavior of the GrIS and its contribution to sea level rise, especially under future high-emissions scenarios.

CRediT authorship contribution statement

Jiahui Qiu: Writing – original draft, Visualization, Software, Methodology, Investigation, Formal analysis, Data curation, Conceptualization. **Jiangjun Ran:** Writing – review & editing, Supervision, Resources, Funding acquisition, Formal analysis, Conceptualization. **Natthachet Tangdamrongsub:** Writing – review & editing. **Xavier Fettweis:** Writing – review & editing, Resources. **Shoaib Ali:** Writing – review & editing. **Wei Feng:** Writing – review & editing. **Xiaoyun Wan:** Writing – review & editing.

Declaration of competing interest

The authors declare that they have no known competing financial interests or personal relationships that could have appeared to influence the work reported in this manuscript. All the authors listed have approved the manuscript that is enclosed.

Acknowledgments

We would like to thank the editors and all the anonymous reviewers for their constructive and insightful comments on the earlier drafts of this manuscript. This study was supported by the National Natural Science Foundation of China (Grant Nos. 42174096, 42322403) and the Asian Institute of Technology (AIT) Research Initiation Grant (No. SET 2023-006). We also acknowledge the support from Center for Computational Science and Engineering at Southern University of Science and Technology.

Appendix A. Supplementary data

Supplementary data to this article can be found online at https://doi.org/10.1016/j.rse.2025.114896.

Data availability

All remotely sensed datasets used in this study are open access (see Sect. 3). SGL area time series with uncertainty in this study can be found at https://zenodo.org/record/13924069. Deep learning-based architecture code and JavaScript code processed on GEE will be made available on request.

References

Andrews, L.C., Catania, G.A., Hoffman, M.J., Gulley, J.D., Lüthi, M.P., Ryser, C., Hawley, R.L., Neumann, T.A., 2014. Direct observations of evolving subglacial drainage beneath the Greenland ice sheet. Nature 514, 80–83.

Badrinarayanan, V., Kendall, A., Cipolla, R., 2017. SegNet: a deep convolutional encoder-decoder architecture for image segmentation. IEEE Trans. Pattern Anal. Mach. Intell. 39, 2481–2495.

Banwell, A.F., Willis, I.C., Macdonald, G.J., Goodsell, B., MacAyeal, D.R., 2019. Direct measurements of ice-shelf flexure caused by surface meltwater ponding and drainage. Nat. Commun. 10, 1–10.

Bell, R.E., Chu, W., Kingslake, J., Das, I., Tedesco, M., Tinto, K.J., Zappa, C.J., Frezzotti, M., Boghosian, A., Lee, W.S., 2017. Antarctic ice shelf potentially stabilized by export of meltwater in surface river. Nature 544, 344–348.

Benedek, C.L., Willis, I.C., 2021. Winter drainage of surface lakes on the Greenland ice sheet from Sentinel-1 SAR imagery. Cryosphere 15, 1587–1606.

Benn, D.I., Cowton, T., Todd, J., Luckman, A., 2017. Glacier calving in Greenland. Curr. Clim. Chang. Rep. 3, 282–290.

van den Berk, J., Drijfhout, S.S., Hazeleger, W., 2021. Circulation adjustment in the Arctic and Atlantic in response to Greenland and Antarctic mass loss. Clim. Dyn. 57, 1689–1707.

Beyer, S., Kleiner, T., Aizinger, V., Rückamp, M., Humbert, A., 2018. A confined–unconfined aquifer model for subglacial hydrology and its application to the Northeast Greenland ice stream. Cryosphere 12 (12), 3931–3947.

van den Broeke, M.R., Enderlin, E.M., Howat, I.M., Kuipers Munneke, P., Noël, B.P.Y., van de Berg, W.J., van Meijgaard, E., Wouters, B., 2016. On the recent contribution of the Greenland ice sheet to sea level change. Cryosphere 10, 1933–1946.

Chen, C., Howat, I.M., De la Pena, S., 2017. Formation and development of supraglacial lakes in the percolation zone of the Greenland ice sheet. J. Glaciol. 63, 847–853.

Chen, Z., Chi, Z., Zinglersen, K.B., Tian, Y., Wang, K., Hui, F., Cheng, X., 2020. A new image mosaic of Greenland using Landsat-8 OLI images. Sci. Bull. 65, 522–524.

Christoffersen, P., Bougamont, M., Hubbard, A., Doyle, S.H., Grigsby, S., Pettersson, R., 2018. Cascading lake drainage on the Greenland ice sheet triggered by tensile shock and fracture. Nat. Commun. 9, 1064.

Chu, V., 2014. Greenland ice sheet hydrology: a review. Prog. Phys. Geogr. 38, 19–54.

Chudley, T.R., Christoffersen, P., Doyle, S.H., Bougamont, M., Schoonman, C.M., Hubbard, B., James, M.R., 2019. Supraglacial lake drainage at a fast-flowing Greenlandic outlet glacier. Proc. Natl. Acad. Sci. USA 116, 25468–25477.

Colgan, W., Steffen, K., McLamb, W.S., Abdalati, W., Rajaram, H., Motyka, R., Phillips, T., Anderson, R., 2011. An increase in crevasse extent, West Greenland: hydrologic implications. Geophys. Res. Lett. 38, 113–120.

Datta, R.T., Wouters, B., 2021. Supraglacial lake bathymetry automatically derived from ICESat-2 constraining lake depth estimates from multi-source satellite imagery. Cryosphere 15, 5115–5132.

Dell, R.L., Banwell, A.F., Willis, I.C., Arnold, N.S., Halberstadt, A.R.W., Chudley, T.R., Pritchard, H.D., 2021. Supervised classification of slush and ponded water on Antarctic ice shelves using Landsat 8 imagery. J. Glaciol. 68 (268), 401–414.

Diakogiannis, F.I., Waldner, F., Caccetta, Peter, Wu, C., 2020. ResUNet-a: A deep learning framework for semantic segmentation of remotely sensed data. Isprs J. Photogramm. 162, 94–114.

Dirscherl, M., Dietz, A.J., Kneisel, C., Kuenzer, C., 2020. Automated mapping of Antarctic supraglacial lakes using a machine learning approach. Remote Sens. 12, 1203.

Dirscherl, M.C., Dietz, A.J., Kuenzer, C., 2021. Seasonal evolution of Antarctic supraglacial lakes in 2015–2021 and links to environmental controls. Cryosphere 15, 5205–5226.

Dow, C.F., Kulessa, B., Rutt, I.C., Tsai, V.C., Pimentel, S., Doyle, S.H., van As, D., Lindbäck, K., Pettersson, R., Jones, G.A., Hubbard, A., 2015. Modeling of subglacial hydrological development following rapid supraglacial lake drainage. Case Rep. Med. 120, 1127–1147.

Fair, Z., Flanner, M., Brunt, K.M., Fricker, H.A., Gardner, A., 2020. Using ICESat-2 and operation IceBridge altimetry for supraglacial lake depth retrievals. Cryosphere 14 (11), 4253–4263.

Fettweis, X., Tedesco, M., van den Broeke, M., Ettema, J., 2011. Melting trends over the Greenland ice sheet (1958–2009) from spaceborne microwave data and regional climate models. Cryosphere 5, 359–375.

Fettweis, X., Box, J.E., Agosta, C., Amory, C., Kittel, C., Lang, C., van As, D., Machguth, H., Gallée, H., 2017. Reconstructions of the 1900-2015 Greenland ice sheet surface mass balance using the regional climate MAR model. Cryosphere 11, 1015–1033.

Fettweis, X., Hofer, S., Krebs-Kanzow, U., Amory, C., Aoki, T., Berends, C.J., Born, A., Box, J.E., Delhasse, A., Fujita, K., Gierz, P., Goelzer, H., Hanna, E., Hashimoto, A., Huybrechts, P., Kapsch, M.-L., King, M.D., Kittel, C., Lang, C., Langen, P.L., Lenaerts, J.T.M., Liston, G.E., Lohmann, G., Mernild, S.H., Mikolajewicz, U., Modali, K., Mottram, R.H., Niwano, M., Noël, B., Ryan, J.C., Smith, A., Streffing, J., Tedesco, M., van de Berg, W.J., van den Broeke, M., van de Wal, R.S.W., van Kampenhout, L., Wilton, D., Wouters, B., Ziemen, F., Zolles, T., 2020. GrSMBMIP: intercomparison of the modelled 1980–2012 surface mass balance over the Greenland ice sheet. Cryosphere 14, 3935–3958.

Fricker, H.A., Arndt, P., Brunt, K.M., Datta, R.T., Fair, Z., Jasinski, M.F., Kingslake, J., Magruder, L.A., Moussavi, M., Pope, A., Spergel, J.J., Stoll, J.D., Wouters, B., 2021. ICESat-2 meltwater depth estimates: application to surface melt on Amery ice shelf, East Antarctica. Geophys. Res. Lett. 48 (8) e2020GL090550.

Gardner, A.S., Moholdt, G., Scambos, T., Fahnstock, M., Ligtenberg, S., Van den Broeke, M., Nilsson, J., 2018. Increased West Antarctic and unchanged East Antarctic ice discharge over the last 7 years. Cryosphere 12, 521–547.

Gorelick, N., Hancher, M., Dixon, M., Ilyushchenko, S., Thau, D., Moore, R., 2017. Google earth engine: planetary-scale geospatial analysis for everyone. Remote Sens. Environ. 202, 18–27.

Haacker, J., Wouters, B., Fettweis, X., Glissenaar, I.A., Box, J.E., 2024. Atmospheric-river-induced foehn events drain glaciers on Novaya Zemlya. Nat. Commun. 15 (1), 7021.

Halberstadt, A.R.W., Gleason, C.J., Moussavi, M.S., Pope, A., Trusel, L.D., DeConto, R.M., 2020. Antarctic supraglacial Lake identification using Landsat-8 image classification. Remote Sens. 12, 1327.

Hanna, E., Huybrechts, P., Steffen, K., Cappelen, J., Huff, R., Shuman, C., Irvine-Fynn, T., Wise, S., Griffiths, M., 2008. Increased runoff from melt from the Greenland ice sheet: a response to global warming. J. Clim. 21, 331–341.

Hersbach, H., Bell, B., Berrisford, P., Hirahara, S., Horányi, A., Muñoz-Sabater, J., Nicolas, J., Peubey, C., Radu, R., Schepers, D., Simmons, A., Soci, C., Abdalla, S., Abellan, X., Balsamo, G., Bechtold, P., Biavati, G., Bidlot, J., Bonavita, M., De Chiara, G., Dahlgren, P., Dee, D., Diamantakis, M., Dragani, R., Flemming, J., Forbes, R., Fuentes, M., Geer, A., Haimberger, L., Healy, S., Hogan, R.J., Hólm, E., Janisková, M., Keeley, S., Laloyaux, P., Lopez, P., Lupu, C., Radnoti, G., de Rosnay, P., Rozum, I., Vamborg, F., Villaume, S., Thépaut, J.N., 2020. The ERA5 global reanalysis. Q. J. R. Meteorol. Soc. 146, 1999–2049.

Howat, I.M., Negrete, A., Smith, B.E., 2014. The Greenland ice mapping project (GIMP) land classification and surface elevation data sets. Cryosphere 8, 1509–1518.

Hu, J., Shen, L., Albanie, S., Sun, G., Wu, E., 2020. Squeeze-and-excitation networks. IEEE Trans. Pattern Anal. Mach. Intell. 42, 2011–2023.

Hu, J., Huang, H., Chi, Z., Cheng, X., Wei, Z., Chen, P., Xu, X., Qi, S., Xu, Y., Zheng, Y., 2022. Distribution and evolution of Supraglacial Lakes in Greenland during the 2016–2018 melt seasons. Remote Sens. 14, 55.

Ignéczi, Á., Sole, A.J., Livingstone, S.A., Leeson, A.A., Fettweis, X., Selmes, N., Gourmelen, N., Briggs, K., 2016. Northeast sector of the Greenland ice sheet to undergo the greatest inland expansion of supraglacial lakes during the 21st century. Geophys. Res. Lett. 43, 9729–9738.

Jiang, D., Li, X., Zhang, K., Marinsek, S., Hong, W., Wu, Y., 2022. Automatic supraglacial Lake extraction in Greenland using Sentinel-1 SAR images and attention-based U-net. Remote Sens. 14, 4998.

Kim, Y., Kimball, J.S., Glassy, J., McDonald, K.C., 2021. MEaSUREs Polar EASE-Grid 2.0 Daily 6 km Land Freeze. Thaw Status from AMSR-E and AMSR2, Version, 2.

Lampkin, D.J., Koenig, L., Joseph, C., Box, J.E., Carr, R.J., Lampkin, D.J., 2020. Investigating controls on the formation and distribution of wintertime storage of water in supraglacial lakes. Front. Earth Sci. 8, 370.

Li, R., Liu, W., Yang, L., Sun, S., Hu, W., Zhang, F., Li, W., 2017. DeepUNet: a deep fully convolutional network for pixel-Level Sea-land segmentation. IEEE J. Sel. Top. Appl. Earth Obs. Remote Sens. 11, 3954–3962.

Li, Y., Yang, K., Gao, S., Smith, L.C., Fettweis, X., Li, M., 2022. Surface meltwater runoff routing through a coupled supraglacial-proglacial drainage system, Inglefield land, Northwest Greenland. Int. J. Appl. Earth Obs. 106, 102647.

Liu, W., Chen, X., Ran, J., Liu, L., Wang, Q., Xin, L., Li, G., 2021. LaeNet: a novel lightweight multitask CNN for automatically extracting Lake area and shoreline from remote sensing images. Remote Sens. 13, 56.

Lüthje, M., Pedersen, L.T., Reeh, N., Greuell, W., 2006. Modeling the evolution of supraglacial lakes on the West Greenland ice-sheet margin. J. Glaciol. 52, 608–618.

Miles, K.E., Willis, I.C., Benedek, C.L., Williamson, A.G., Tedesco, M., 2017. Toward monitoring surface and subsurface lakes on the Greenland ice sheet using Sentinel-1 SAR and Landsat-8 OLI imagery. Front. Earth Sci. 5, 58.

Mohajerani, S., Saeedi, P., 2019. Cloud-net: an end-to-end cloud detection algorithm for Landsat 8 imagery. Int. Geosci. Remote Sens. Symp. (IGARSS) 1029–1032.

Moon, T.A., Mankoff, K.D., Fausto, R.S., Fettweis, X., Loomis, B.D., Mote, T.L., Poinar, K., Tedesco, M., Wehrlé, A., Jensen, C.D., 2022. Arctic Report Card 2022: Greenland Ice Sheet. https://doi.org/10.25923/c430-hb50.

Moussavi, M., Pope, A., Halberstadt, A.R.W., Trusel, L.D., Cioffi, L., Abdalat, W., 2020. Antarctic supraglacial lake detection using Landsat 8 and Sentinel-2 imagery: towards continental generation of lake volumes. Remote Sens. 12, 134.

Nienow, P.W., Sole, A.J., Slater, D.A., Cowton, T.R., 2017. Recent advances in our understanding of the role of meltwater in the Greenland ice sheet system. Curr. Clim. Chang. Rep. 3, 330–344.

Otsu, N., 1979. A threshold selection method from gray-level histograms. IEEE Trans. Syst. Man Cybern. 9, 62–66.

Ouyang, S., Li, Y., 2021. Combining deep semantic segmentation network and graph convolutional neural network for semantic segmentation of remote sensing imagery. Remote Sens. 13, 119.

Pekel, J.-F., Cottam, A., Gorelick, N., Belward, A.S., 2016. High-resolution mapping of global surface water and its long-term changes. Nature 540, 418–422.

Pi, X., Luo, Q., Feng, L., Xu, Y., Tang, J., Liang, X., Ma, E., Cheng, R., Fensholt, R., Brandt, M., 2022. Mapping global lake dynamics reveals the emerging roles of small lakes. Nat. Commun. 13, 5777.

Pitcher, L.H., Smith, L.C., 2019. Supraglacial streams and Rivers. Annu. Rev. Earth Planet. Sci. 47, 421–452.

Pope, A., 2016. Reproducibly estimating and evaluating supraglacial lake depth with Landsat 8 and other multispectral sensors. Earth Space Sci. 3, 176–188.

Porter, C., Morin, P., Howat, I., Noh, M.-J., Bates, B., Peterman, K., Keesey, S., Schlenk, M., Gardiner, J., Tomko, K., Willis, M., Kelleher, C., Cloutier, M., Husby, E., Foga, S., Nakamura, H., Platson, M., Wethington, Michael, Williamson, C., Bauer, G., Enos, J., Arnold, G., Kramer, W., Becker, P., Doshi, A., D'Souza, C., Cummens, P., Laurier, F., Bojesen, M., 2018. ArcticDEM, Version 3, Harvard Dataverse. https://doi.org/10.7910/DVN/OHHUKH.

Previdi, M., Smith, K.L., Polvani, L.M., 2021. Arctic amplification of climate change: a review of underlying mechanisms. Environ. Res. Lett. 16, 093003.

Ran, J., Vizcaino, M., Ditmar, P., van den Broeke, M.R., Moon, T., Steger, C.R., Enderlin, E.M., Wouters, B., Noël, B., Reijmer, C.H., Klees, R., Zhong, M., Liu, L., Fettweis, X., 2018. Seasonal mass variations show timing and magnitude of meltwater storage in the Greenland ice sheet. Cryosphere 12, 2981–2999.

Ran, J., Ditmar, P., van den Broeke, M.R., Liu, L., Klees, R., Khan, S.A., Moon, T., Li, J., Bevis, M., Zhong, M., Fettweis, X., Liu, J., Noël, B., Shum, C.K., Chen, J., Jiang, L., van Dam, T., 2024. Vertical bedrock shifts reveal summer water storage in Greenland ice sheet. Nature 635 (8037), 108–113.

Reichstein, M., Camps-Valls, G., Stevens, B., Jung, M., Denzler, J., Carvalhais, N., Prakash, P., 2019. Deep learning and process understanding for data-driven earth system science. Nature 566, 195–204.

Rignot, E., Mouginot, J., 2012. Ice flow in Greenland for the international polar year 2008–2009. Geophys. Res. Lett. 39, L11501. https://doi.org/10.1029/2012GL051634.

Ronneberger, O., Fischer, P., Brox, T., 2015. U-net: convolutional networks for biomedical image segmentation. Lect. Notes Comput. Sci 9351, 234–241.

Salerno, F., Thakuri, S., D'Agata, C., Smiraglia, C., Manfredi, E.C., Viviano, G., Tartari, G., 2012. Glacial lake distribution in the Mount Everest region: uncertainty of measurement and conditions of formation. Glob. Planet. Chang. 92–93, 30–39.

Sasgen, I., Wouters, B., Gardner, A.S., King, M.D., Tedesco, M., Landerer, F.W., Dahle, C., Save, H., Fettweis, X., 2020. Return to rapid ice loss in Greenland and record loss in 2019 detected by the GRACE-FO satellites. Commun. Earth Environ. 1 (1), 8.

Schröder, L., Neckel, N., Zindler, R., Humbert, A., 2020. Perennial supraglacial lakes in Northeast Greenland observed by polarimetric SAR. Remote Sens. 12, 2798.

Selmes, N., Murray, T., James, T.D., 2011. Fast draining lakes on the Greenland ice sheet. Geophys. Res. Lett. 38, 165–176.

Smith, L.C., Yang, K., Pitcher, L.H., Overstreet, B.T., Chu, V.W., Rennermalm, Å.K., Ryan, J.C., Cooper, M.G., Gleason, C.J., Tedesco, M., Jeyaratnam, J., Van As, D., Van den Broeke, M.R., Van De Berg, W.J., Noël, B., Langen, P.L., Cullather, R.I., Zhao, B., Willis, M.J., Behar, A.E., 2017. Direct measurements of meltwater runoff on the Greenland ice sheet surface. Proc. Natl. Acad. Sci. USA 114, E10622–E10631.

Stevens, L.A., Behn, M.D., McGuire, J.J., Das, S.B., Joughin, I., Herring, T., Shean, D.E., King, M.A., 2015. Greenland supraglacial lake drainages triggered by hydrologically induced basal slip. Nature 522, 73–76.

Stokes, C.R., Sanderson, J.E., Miles, B., Jamieson, S.S.R., Leeson, A., 2019. Widespread distribution of supraglacial lakes around the margin of the East Antarctic ice sheet. Sci. Rep. 9, 13823.

Sundal, A.V., Shepherd, A., Nienow, P., Hanna, E., Palmer, S., Huybrechts, P., 2009. Evolution of supra-glacial lakes across the Greenland ice sheet. Remote Sens. Environ. 113, 2164–2171.

Tedesco, M., Lthje, M., Steffen, K., Steiner, N., Fettweis, X., Willis, I., Bayou, N., Banwell, A., 2012. Measurement and modeling of ablation of the bottom of supraglacial lakes in western Greenland. Geophys. Res. Lett. 39, L02502.

Turton, J.V., Hochreuther, P., Reimann, N., Blau, M.T., 2021. The distribution and evolution of supraglacial lakes on 79°N glacier (North-Eastern Greenland) and interannual climatic controls. Cryosphere 15, 3877–3896.

van de Wal, R.S.W., Boot, M., van den Broeke, M.R., Smeets, C.J.P.P., Reijmer, C.H., Donker, J.J.A., Oerlemans, J., 2008. Large and rapid melt-induced velocity changes in the ablation zone of the Greenland ice sheet. Science 321, 111–113.

Wang, M., Chen, Y., Qi, B., 2022. Residual UNet with spatial and channel attention for automatic magnetic resonance image segmentation of rectal cancer. Multimed. Tools Appl. 81, 43821–43835.

Weiss, M., Jacob, F., Duveiller, G., 2020. Remote sensing for agricultural applications: a meta-review. Remote Sens. Environ. 236, 111402.

Williams, J.J., Gourmelen, N., Nienow, P., 2020. Dynamic response of the Greenland ice sheet to recent cooling. Sci. Rep. 10 (1), 1647.

Williamson, A.G., Arnold, N.S., Banwell, A.F., Willis, I.C., 2017. A fully automated supraglacial lake area and volume tracking ("FAST") algorithm: development and application using MODIS imagery of West Greenland. Remote Sens. Environ. 196, 113–133.

Williamson, A.G., Banwell, A.F., Willis, I.C., Arnold, N.S., 2018. Dual-satellite (Sentinel-2 and Landsat 8) remote sensing of supraglacial lakes in Greenland. Cryosphere 12, 3045–3065.

Yang, K., Li, M., 2014. Greenland ice sheet surface melt: a review. Sci. Cold Arid Reg. 6, 99–106.

Yang, K., Smith, L.C., 2013. Supraglacial streams on the Greenland ice sheet delineated from combined spectral-shape information in high-resolution satellite imagery. IEEE Geosci. Remote Sens. Lett. 10, 801–805.

Yang, K., Smith, L.C., Karlstrom, L., Cooper, M.G., Tedesco, M., van As, D., Cheng, X., Chen, Z., Li, M., 2018. A new surface meltwater routing model for use on the Greenland ice sheet surface. Cryosphere 12, 3791–3811.

Yuan, J., Chi, Z., Cheng, X., Zhang, T., Li, T., Chen, Z., 2020. Automatic extraction of Supraglacial Lakes in Southwest Greenland during the 2014–2018 melt seasons based on convolutional neural network. Water 12, 891.

Zhang, E., Liu, L., Huang, L., Ng, K.S., 2021. An automated, generalized, deep-learning-based method for delineating the calving fronts of Greenland glaciers from multi-sensor remote sensing imagery. Remote Sens. Environ. 254, 112265.

Zhang, G., Bolch, T., Yao, T., Rounce, D.R., Chen, W., Veh, G., King, O., Allen, S.K., Wang, M., Wang, W., 2023. Underestimated mass loss from lake-terminating glaciers in the greater Himalaya. Nat. Geosci. 16, 333–338.

Zhao, S., Hao, G., Zhang, Y., Wang, S., 2021. A real-time semantic segmentation method of sheep carcass images based on ICNet. J. Robot. 2021, 1–12.

Zheng, L., Li, L., Chen, Z., He, Y., Mo, L., Chen, D., Hu, Q., Wang, L., Liang, Q., Cheng, X., 2023. Multi-sensor imaging of winter buried lakes in the Greenland ice sheet. Remote Sens. Environ. 295, 113688.

Zhou, Z., Rahman Siddiquee, M.M., Tajbakhsh, N., Liang, J., 2019. Unet++: redesigning skip connections to exploit multiscale features in image segmentation. IEEE Trans. Med. Imaging 39 (6), 1856–1867.

Zwally, H.J., Abdalati, W., Herring, T., Larson, K., Saba, J., Steffen, K., 2002. Surface melt-induced acceleration of Greenland ice-sheet flow. Science 297, 218–222.